Natural Resources Research (© 2017)
https://doi.org/10.1007/s11053-017-9360-5

Original Paper

Identifying Groundwater Potential in Crystalline Basement Rocks Using Remote Sensing and Electromagnetic Sounding Techniques in Central Western Mozambique

Luís André Magaia,[1,2] Tada-nori Goto,[1] Alaa Ahmed Masoud,[3] and Katsuaki Koike[1,4]

Received 16 August 2017; accepted 14 November 2017

Exploring for groundwater in crystalline rocks in semiarid areas is a challenge because of their complex hydrogeology and low potential yields. An integrated approach was applied in central western Mozambique, in an area covered by Precambrian crystalline basement rocks. The approach combined a digital elevation model (DEM), remote sensing, and a ground-based geophysical survey. The aim was to identify groundwater zones with high potential and to identify geological structures controlling that potential. Lineaments were extracted from the DEM that had been enhanced using an adaptive-tilt, multi-directional, shading technique and a non-filtering technique to characterize the regional fracture system. The shallowness and amount of stored groundwater in the fracture zones was assessed using vegetation indices derived from Landsat 8 OLI images. Then, 14 transient electromagnetic (TEM) survey profiles were taken in different geological settings across continuous lineaments that were considered to be aligned along inferred faults. In the central lineament zones, the TEM soundings gave resistivity values of less than 300 Ωm at a depth of 20–80 m. The values varied with location. Conversely, values greater than 400 Ωm were observed at the sites away from the central zones. This contrast is probably caused by the differences in permeability and degree of weathering along the fractured zones. These differences could be key factors in determining groundwater occurrence. By integrating five water-related factors (lineament density, slope, geology, vegetation index, and proximity to lineaments), high groundwater potential zones were located in the vicinity of the lineaments. In these zones, vegetation remains active regardless of the season.

KEY WORDS: Digital elevation model, Lineament, Landsat 8 OLI image, Vegetation index, Transient electromagnetic method, Crystalline basement.

INTRODUCTION

Groundwater in crystalline rocks mainly occurs in shallow weathered zones of limited narrow extent. Groundwater productivity in crystalline rocks is typically low and dependent on the thickness and width of the weathered and fractured crystalline bedrock (e.g., Wright 1992; Chilton and Foster 1995). Because fracture zones are mechanically weak and foci for weathering, they can store and

[1]Department of Urban Management, Graduate School of Engineering, Kyoto University, Kyoto 615-8540, Japan.
[2]Geology Department, Faculty of Sciences, Eduardo Mondlane University, Ave. Mozambique km 1.5, P.O. Box 257, Maputo, Mozambique.
[3]Geology Department, Faculty of Science, Tanta University, Tanta 31527, Egypt.
[4]To whom correspondence should be addressed; e-mail: koike.katsuaki.5x@kyoto-u.ac.jp

Published online: 27 November 2017

transmit more groundwater than intact rocks and form the main aquifers. Abundant, uniform vegetation can be found along fracture zones, which are associated with the development of specific soil types because of the chemical interactions between the soil and the relatively abundant groundwater (Ruland et al. 1991; Wang et al. 2013). Development of groundwater from such aquifers has high risk of failure because of low drilling success ratio in such complex hydrogeological conditions.

Because fracture zones are selectively eroded, they tend to appear as lineaments on satellite remote sensing images. Therefore, satellite images can provide useful information, over wide areas, on regional fracture systems that are sometimes inaccessible to ground surveys, or shown in insufficient detail in geological maps and investigation data (Shaban et al. 2006; Sander 2007; Mallast et al. 2011). In addition, because relatively abundant groundwater causes high vegetation activity, the physiological activity of vegetation can be estimated using reflectance data acquired as optical sensor images. Another powerful tool in groundwater surveys is geophysical mapping the effects of water content on physical properties of rocks, such as resistivity. Water-filled fractures may be detected by electromagnetic methods because resistivity lower than intact rock is attributed to conductive ions in water, the connectivity of fractures, and conductive clay minerals present as fracture linings or as alteration products in the surrounding rocks (e.g., National Research Council 1996). The resultant property distribution can show lateral and vertical extents of the groundwater potential. For the purposes of this paper, we define groundwater potential as the aquifer state that can provide at least 900 l/h throughout the year. A combination of geophysical data and typical optical sensor satellite imagery (e.g., Landsat) has been proven to be effective for mapping potential groundwater zones in areas where weathering has selectively progressed as a result of the control of dominant structural trends (Ranganai and Ebinger 2008; Tessema et al. 2012). Thus, integration of multiple-type data can enable the production of accurate maps of groundwater potential, allow the identification of high potential zones, and provide a basis for groundwater resource management and planning.

This study aims to develop a method of integrating remotely sensed and near surface geophysical data for regional groundwater exploration in semiarid areas with crystalline basement rocks and regolith. Central western Mozambique was chosen as the case study area. Lineament extraction from a digital elevation model (DEM), a vegetation index derived from Landsat 8 OLI images, and transient electromagnetic (TEM) survey data were integrated. ArcGIS 10.2.2 was used to georeference and overlay these datasets. The technique will contribute to groundwater exploration of deep-seated aquifers in basement rocks covered by a highly fractured and weathered overburden. This is likely the first study that successfully combines TEM surveying with remotely sensed image analysis of vegetation index and lineaments for assessment of potential groundwater resources in Precambrian crystalline areas of Africa.

STUDY AREA

The study area covers about 2000 km^2 in the northeast of Tete Province in Mozambique, encompassing the eastern side of the Angonia District and the northeastern corner of the Tsangano District from S14°27′50″ to S14°53′00″ and E34°09′30″ to E34°34′30″ (Fig. 1). The study area is contiguous to Malawi in the east. Ulongue village, in the middle of the study area, is 230 km from the capital city, Tete, the largest urban area. Angonia is the most populated district in the province with a population density of 101 people/km^2 and, as in the other districts, suffers from a lack of sustainable water resources. The region is highly productive in terms of crops because of the moderate climate. Crop production is the main economic activity followed by cattle farming. According to the Meteorology Institute of Mozambique, the mean annual precipitation from 1965 to 1984 in Ulongue was 905 mm; the rainy season is between December and the following March, with a mean of 200 mm.

The morphology of the area is characterized by extensive plateaus and mountains with variable elevations (from 0.7 to 2 km a.s.l.) as well as inselbergs or residual hills in places, long valleys, and plains. The study area is chiefly founded on crystalline basement complex rocks from the Mesoproterozoic and Neoproterozoic eras. High-grade metamorphic rocks are dominated by gneiss and gneiss–granite–migmatite, with local metasediments, charnockite, and gabbro–anorthosite (Lächelt 2004; CGS 2007) (Fig. 1).

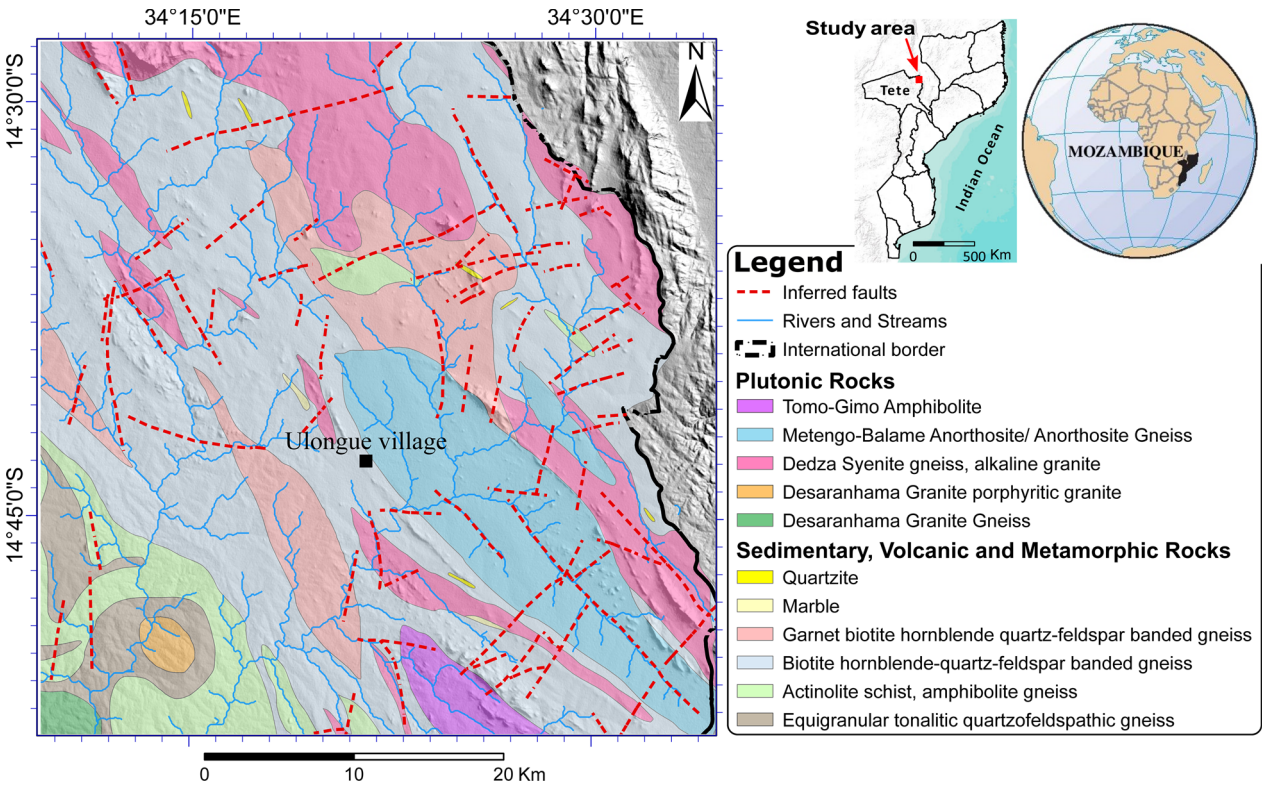

Figure 1. Location of the study area in Tete Province, central western Mozambique, and a simplified geological map digitized from the 1:250,000 scale map (DNG 2006) with SRTM (Shuttle Radar Topographic Mission) DEM (gray shading) as a backdrop. Malawi is indicated by the absence of a geological map.

MATERIALS AND METHODS

Remotely Sensed Data

Lineament analysis using DEM can consider topographic features more directly than satellite imagery that has a brightness bias because of the sun's illumination effect, surface cover materials, and artificial structures. Therefore, one scene of the 3-arc second DEM data from Shuttle Radar Topographic Mission (SRTM) from Jarvis et al. (2008), SRTM 43_15 with 90-m grid spacing, was selected. In addition, more precise SRTM DEM with 1-arc second and 30-m grid spacing, S15_E034_1arc_v3, was used for river and stream extraction, and for topographic correction of the solar illumination effect in the Landsat Operational Land Imager (OLI) images. To compare vegetation indices for the dry and wet seasons, two OLI row 70/path 168 scenes in L1T mode were selected (Table 1). These datasets were georeferenced to Zone 36 South of the Universal Transverse Mercator coordinate system based on the WGS datum of 1984. The images were processed using ENVI software. To derive surface reflectance from the images, Digital Numbers (DN) of the images were first converted into radiance data, and then atmospheric and radiometric corrections were applied using Fast Line-of-sight Atmospheric Analysis of Spectral Hypercubes (FLAASH) (Matthew et al. 2000). This transformed the radiance of each pixel into reflectance based on local atmospheric conditions. The parameter model in the FLAASH module was based on a tropical atmosphere and rural aerosol conditions with 2-band (K-T) aerosol retrieval.

Image processing with topographic normalization was then applied using the method of Civco (1989). This corrected the brightness distortion caused by the irregular shape of the terrain using the above 1-arc second STRM DEM for the incident angle (γ_i) of an illumination model (II) following:

Table 1. Specification of Landsat 8 OLI scenes used in this study

	Acquisition date	Scene center time	Cloud cover	Sun azimuth angle	Sun elevation angle
1	27 Apr. 2015	07:46:03	0.1%	46.4°	50°
2	18 Sep. 2015	07:46:43	0%	61.3°	58.1°

$$Il = \cos\gamma_i = \cos\theta_p \cos\theta_z + \sin\theta_p \sin\theta_z \cos(\phi_a - \phi_o) \quad (1)$$

where θ_p, θ_z, ϕ_a, and ϕ_o are the angles of the slope, solar zenith, solar azimuth, and aspect, respectively. Then the C-correction method, a non-Lambertian technique, was applied to compute the horizontal reflectance image, ρ_H (Teillet et al. 1982):

$$\rho_H = \rho_T \left(\frac{\cos\theta_z + c_k}{Il + c_k} \right) \quad (2)$$

where ρ_T is the reflectance of an inclined surface and c_k is a coefficient to relate ρ_T at a band k to Il by a linear regression $\rho_T = b_k + m_k Il$, where b_k and m_k are the regression coefficients and $c_k = b_k/m_k$.

Lineament Extraction

Lineaments that correspond with fractures promote deeper weathering of the overburden and act as paths for water infiltration and groundwater flow. Their extraction from the interpretation of air photographs, satellite images, or DEM images requires skill and time, and the resultant number, location, length, and orientation of extracted lineaments depend on the photograph/image quality and the researcher's subjective interpretation. To avoid these problems, we adopted an automatic and non-filtering approach: segment tracing algorithm (STA) (Koike et al. 1995). This approach has the advantage of extracting interconnected lineaments by tracing only continuous valleys from low brightness contrast and small topographic relief areas. The merits of this approach have been demonstrated by multiple case studies of regional fracture-system characterization in the fields of geodynamics (Masoud and Koike 2011a, b; Wang et al. 2013), hydrogeology (Masoud and Koike 2006), and prospecting (vein-type metal deposits) (Koike et al. 1998).

A technique of adaptive-tilt, multi-directional shading (ATMDS) that maximizes the reflectance intensity for illumination at each grid point was developed for STA to extract lineaments from DEM data. Lineaments with similar directions and short distances between end and start points were connected to produce long lineaments of geological significance using B-spline interpolation. Techniques from Masoud and Koike (2011a) were adopted for this study's SRTM DEM using LINDA software (Masoud and Koike 2017).

Vegetation Index

In low precipitation areas, vegetation provides useful information on groundwater occurrence. For example, vegetation cover can help conserve underlying water by reducing the rate of evaporation and erosion, and consequently, enhancing the recharge rate (Saraf and Choudhury 1998; Shaban et al. 2006; Brunner et al. 2007). Vegetation can provide a beneficial covering effect for groundwater. Conversely, the presence of groundwater at shallow depths can provide beneficial effects for vegetation by providing abundant water to support plant growth and vividly colored leaves. The coloration induces strong electromagnetic-wave absorption in the visible red wavelength region, and large wave scattering by the leaf cell structure in the near-infrared wavelength region. This spectral characteristic can be emphasized by a simple band rationing and expressed by an index of vegetation greenness. The Normalized Difference Vegetation Index (NDVI) (Rouse et al. 1974) is the most commonly used index for red band reflectance ρ_{Red} and near-infrared band reflectance ρ_{NIR}:

$$\mathrm{NDVI} = \frac{\rho_{\mathrm{NIR}} - \rho_{\mathrm{Red}}}{\rho_{\mathrm{NIR}} + \rho_{\mathrm{Red}}} \quad (3)$$

When the canopies do not fully cover the ground, the soil reflectance cannot be ignored because its contribution to the total reflectance in each pixel becomes large. Therefore, an additional vegetation index that is less sensitive to the soil background—a Modified Soil Adjusted Vegetation Index (MSAVI) (Qi et al. 1994)—was adopted:

$$\mathrm{MSAVI} = \frac{2\rho_{\mathrm{NIR}} + 1 - \sqrt{(2\rho_{\mathrm{NIR}} + 1)^2 - 8(\rho_{\mathrm{NIR}} - \rho_{\mathrm{Red}})}}{2} \quad (4)$$

Compared with NDVI, MSAVI has been proven to have high signal to noise ratio in arid and sparsely vegetated areas where vegetation cover is less than 25% (Qi et al. 1994; Rondeaux et al. 1996).

Rugged topographic terrains and atmospheric variability also greatly affect vegetation index values (Henebry 1993), and shadows attenuate the index, whereas highly illuminated areas have the opposite effect (Riaño et al. 2003). These problems were minimized by the above topographic normalization in the image preprocessing.

Transient Electromagnetic Method

TEM is a controlled source electromagnetic method that operates at the diffusion regime of electromagnetic waves. A direct current is passed through the transmitting loop laid on the ground surface. At this stage, a static primary magnetic field is generated around the transmitter antenna. When the current is interrupted abruptly, the presence of any conductor body immediately below the surface induces eddy currents and generates a secondary magnetic field as a function of time. The secondary field is measured at the surface by a receiver antenna during the turned-off period when the primary field has deceased as a time-dependent decaying voltage (Nabighian 1991; Reynolds 2011). The decay rate of the secondary magnetic field depends on the bulk resistivity of the measured medium. For interpretation, the measured decaying voltage is converted to apparent resistivity, $\rho_a(t)$:

$$\rho_a(t) = \left(\frac{\sqrt{\pi} \cdot R^4}{20 \cdot S}\right)^{2/3} \left(\frac{\mu_0}{t}\right)^{5/3} \quad (5)$$

where $S = E(t)/I$ is the signal, $E(t)$ is the potential, I is the transmitter current, μ_0 is the magnetic permeability, and $R = L/\sqrt{\pi}$: L is the side length of a square loop for a single coincident loop antenna (Árnason 1989).

One major advantage of TEM is that the signal measurement is carried out during the moment of shut-off current in the transmitting loop and thus no primary field is added to the measurement. Accordingly, the use of the coincident loop antenna makes the survey rapid and cost-effective for determining subsurface resistivity structures. TEM is more sensitive to highly conductive sections of the medium (Fitterman and Stewart 1986; Nabighian 1991). Therefore, TEM sounding is particularly effective for mapping the depth and thickness of good conductors and has been frequently used in hydrological surveys in the USA, Canada, and Europe (e.g., Danielsen et al. 2003; Auken et al. 2006; Sapia et al. 2014; Costabel et al. 2017) as well as Africa (Danielsen et al. 2007; Chongo et al. 2015; Martínez-Moreno et al. 2016). Although direct current (DC) resistivity methods are also frequently used for groundwater studies, TEM has the advantage that the transmitter inductively couples with the ground. High contact resistance in dry resistive terrain often causes problems when using the DC resistivity methods because the exact amount of current injected into the ground is not known. This problem does not apply to the TEM method. The lightweight TEM equipment, compared with DC resistivity equipment, is also a significant advantage.

For the TEM survey, we used the TEM-FAST 48HPC system (Applied Electromagnetic Research) with a single coincident square loop of 20×20 m^2 (Barsukov et al. 2006). To record the decaying voltage, the stack number, the number of time gates, and the transmitting current were set at 130 complete cycles, 32, and 1 A, respectively. When weak signal conditions appeared during the late time of the decaying current, the transmitting current was increased to 4 A. The TEM survey was carried out in September and October 2016, just before the rainy season, at 129 sites along 14 profiles. The resistivity model was obtained by solving the inverse problem in the time domain of electromagnetic soundings using the iterative approach of the Levenberg–Marquardt algorithm and singular value decomposition (Martínez-Moreno et al. 2016). A layered one-dimensional (1-D) resistivity model and cross section from the 1-D models along each profile were constructed using the TEM-Researcher v.8.52 software (Applied Electromagnetic Research) and measured TEM responses at each site. Some data from large noise environments and with large errors were not used for the inversion analysis.

Several datasets were integrated to produce the groundwater potential map; the various stages and the process flow are summarized in Figure 2. The integration process and its verification are discussed in "Assessment of Groundwater Potential" section.

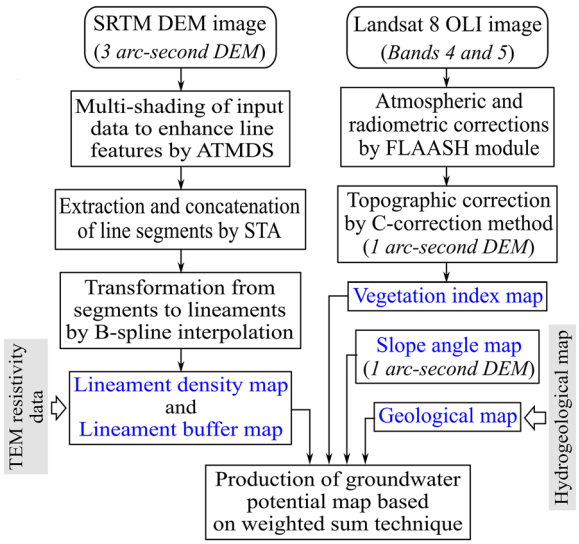

Figure 2. Flowchart showing the integration of five thematic maps (highlighted in blue) to produce the groundwater potential map using a weighted sum technique in a GIS environment. ATMDS: adaptive-tilt multi-directional shading, STA: segment tracing algorithm, FLAASH: Fast Line-of-sight Atmospheric Analysis of Spectral Hypercubes. Input datasets are italicized in brackets, and supporting data are shown in the gray rectangles.

RESULTS

Characterization of Lineament Distribution

In total, 711 lineaments were extracted and overlaid on inferred faults from the geological map by DNG (2006) for comparing their locations, orientations, and lengths (Fig. 3a). As shown by the lineament distribution, the study area is dominated by lineaments along the broadly NNW, NE, and NNE directions (Fig. 3b). Of the 73 inferred faults in the study area, 36% are coincident with the lineaments. Lineaments are distributed all over the area, and 77% lengths are shorter than 5 km. The longest lineaments trend NNW (Fig. 3c) and overlap with the inferred faults (concentrated in the southeast and northeast parts), which confirm the reliability of STA to extract geologically significant lineaments. Most long lineaments also correspond with the long rivers (Fig. 1). Short lineaments, especially those trending NNE, were also found in the Precambrian rocks to the south of the study area (Bicca et al. 2017).

The fault type can be based on the geometrical relationship between the curvature of the grouped lineaments' distribution and the slope dip direction along the lineaments (Masoud and Koike 2011a). The major fault types were strike-slip or undetermined, followed by reverse and normal types (Fig. 4). These types could not be confirmed by the TEM survey. However, the existence of strike-slip shear and thrust fault zones in the east of the study area, inferred from the preceding geological interpretation by field surveys (CGS 2007), could be related to a general characteristic of the fault types' distribution. The mixture of fault types also suggests that different tectonic events occurred in the Mozambique belt (from the Mediterranean Sea to central Mozambique) during the Mozambican tectonic cycle (1350–850 Ma) (Lächelt 2004). The events may have generated different fault systems.

Seasonal Change in the Vegetation Index

Two MSAVI maps from the Landsat 8 scenes for rainy and dry seasons were compared. The results showed that the mountainous areas were dominated by green vegetation with high MSAVI values common to both seasons (Fig. 5). The mountainous areas are located in the eastern side of the study area (along the border with Malawi) and at the north- and southwestern corners of the study area. The lower and central areas are only covered by green vegetation in the rainy season (Fig. 5a). The vegetation cover becomes sparse in the dry season, mainly as a result of the lack of precipitation and the seasonal changes in deciduous vegetation and shrubs. Nevertheless, the zones along the extracted lineaments tend to remain highly vegetated (Fig. 5b).

TEM Resistivity Distribution

Classification into Resistivity Layers

In total, 14 TEM profiles were taken across the lineaments, which had a dominant NNW direction and high MSAVI values, and were mainly aligned along the inferred faults and in different rock types (Fig. 6). The total number of sounding sites was 129, with 6 to 12 sites in each profile. The fault types of the lineaments across which the profiles traverse and the rock types around the profiles are summarized in Table 2. Distributions and depths for 118 wells that supply drinking and irrigation water are also shown in Figure 6, with estimated yields provided by the

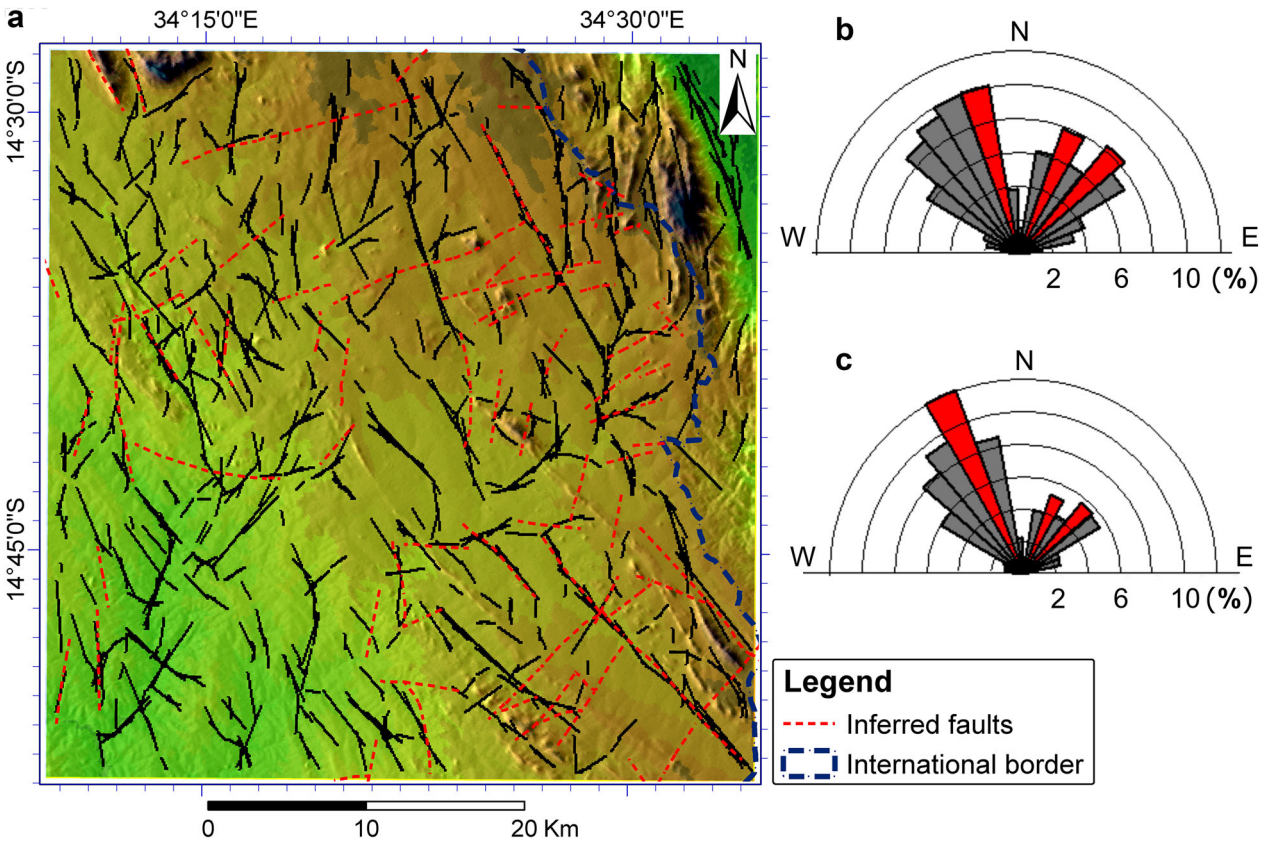

Figure 3. (**a**) Lineaments extracted from multi-shaded SRTM DEM data and overlaid on the shaded relief map, (**b**) rose diagram of frequency of lineament directions, and (**c**) rose diagram using total lineament lengths in each direction sector. Red sectors indicate relatively dominant directions.

Water and Sanitation Division of Tete Province. From six out of the seven wells drilled in 2014 (BH1 to BH7 in Fig. 6), the existence of a weathered gneiss layer within 10 m of the surface was confirmed. In BH5, alternating sediments were found at 0–5 m, weathered gneiss at 5–15 m, and fractured gneiss from 15 to 30 m (Fig. 8b). The weathered gneiss layer was not found in BH6 (total depth = 24 m), and a moderate yield of 1900 l/h was intercepted at the contact between the overlying sediments and the fractured gneiss layer. Well BH1, located 2.3 km southeast of BH6 is in an inferred fault and has a moderate estimated yield of 1800 l/h and is 30 m deep. The results of the well investigations revealed local changes in the degree of weathering and depth to the top of fresh (fractured) basement rocks.

TEM apparent resistivity (ρ_a) curves, plotted on a double logarithmic graph, show different features inside and outside the lineament zones. Inside these zones, the apparent resistivity tends to be relatively low (in general <80 Ωm at shallow depths) (Fig. 7a). This trend becomes more pronounced at the sites in the plutonic rocks, e.g., at site MBA 4 in profile 8, where ρ_a has a minimum close to 10 Ωm at 20 µs (Fig. 7a); its resistivity subsequently increases with time and reaches its maximum at around 400 µs. The ρ_a curves at the sites in the sedimentary rocks, e.g. LAM 6 (Fig. 7a), are almost constant in early times (<100 µs), then decrease steadily, and reach a minimum at late times. In contrast, the ρ_a values at the sites outside the lineament zones become high in early times (peak values >100 Ωm at 10–30 µs), followed by a steady decrease with increasing time (Fig. 7b). These ρ_a characteristics were probably caused by differences in the degree of weathering and permeability, which were enhanced by fracturing. Thus, the lineaments can be used as a fracturing indicator.

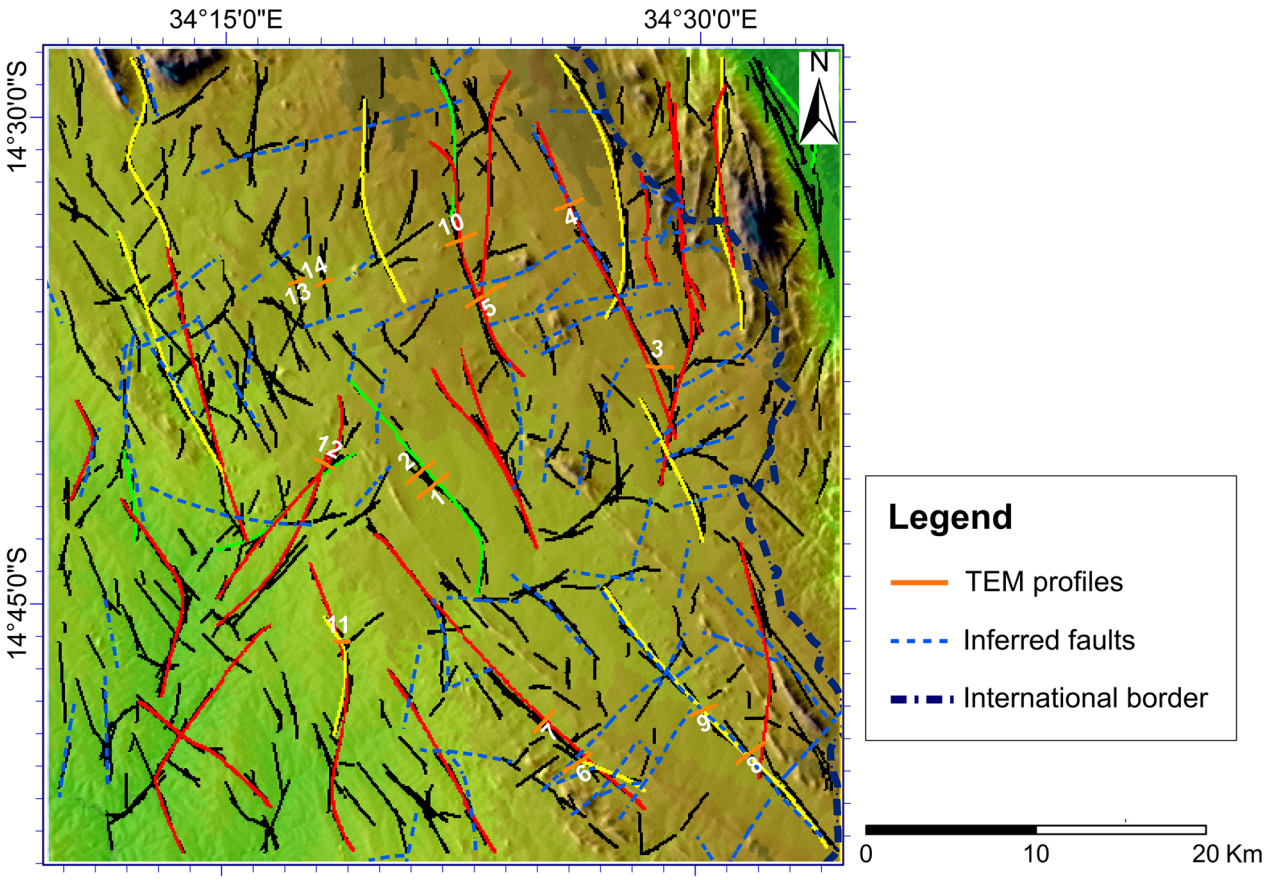

Figure 4. Distribution of long lineaments classified into three fault types (green: normal, yellow: reverse, and red lines: strike-slip) based on a geometrical relationship between the curvature of grouped lineaments' distribution and the slope dip direction along the lineaments (Masoud and Koike 2011a).

The fit between the ρ_a data and the resistivity curves (Figs. 7 and 8a) calculated by the inversion shows that, for most of the sounding sites, the misfits are small enough to be acceptable. The lowest misfit error was 1% at a sounding site in the sedimentary rock, whereas the greatest misfit was 14% in three sites on profile 9. To simplify the model, the minimum number of layers was selected as the best resistivity model at each site for the same misfit. The average misfit error for all sites was 6%.

To interpret the TEM resistivity results in detail, typical resistivity data at a sounding site outside the lineament zone (CHI 1 on the profile 11) were used for a TEM standard sounding curve, and the resultant 1-D resistivity (ρ) model was evaluated (Figs. 6 and 10). The model was roughly classified into four parts from the top downwards: layer I, with low to moderate ρ (4–12 Ωm) and a maximum thickness of 5 m; layer II, a highly resistive layer ($\rho \geq 400$ Ωm) with varying thickness from 20 to 80 m; layer III, characterized by moderate ρ from 10 to 300 Ωm; and layer IV, with low ρ (less than 10 Ωm). Although the ρ values of fresh crystalline rocks are generally high, they decrease considerably with increasing water and clay contents as weathering and fracturing progresses, which can explain the difference in ρ values of the four layers. The four layers were compared with a geological column at BH5 (Fig. 8b). Layer I was assumed to correspond to the surface layer of alternating sediments that have low ρ as a result of the formation of clay minerals. Layer II can be correlated with the less weathered and fractured gneiss layer where ρ is increased as a result of the low water content. The porosity of layer II can be estimated by Archie's law (Archie 1942): $\rho_r = \rho_w \varphi^{-n}$, where ρ_r is the bulk resistivity of water-saturated rock, ρ_w is the pore water resistivity, φ is the porosity, and n is the cementation factor (ap-

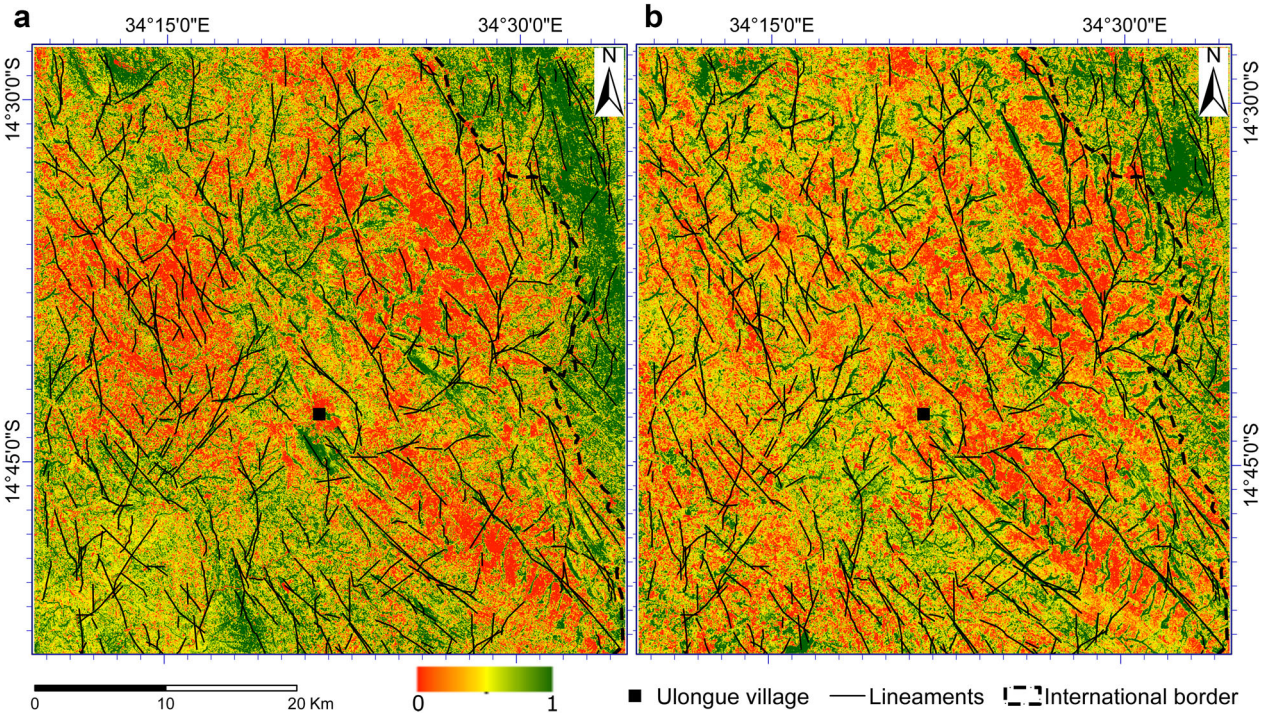

Figure 5. Maps of MSAVI values from two Landsat 8 OLI scenes for (**a**) the end of the rainy season and (**b**) the end of the dry season (Table 1). The maps are normalized to a common range value for comparison and overlaid on the lineaments.

proximately 1.5; National Research Council 1996). Based on data from 118 wells in the study area, the average ρ_w was about 43 Ωm. By assuming a simple aquifer through which perfectly connected fractures pass (i.e., $n = -1$), then ρ of layer II (≥ 400 Ωm) is equivalent to that of rocks with low porosity (≤ about 11%). This condition suggests a low potential yield. The hydrogeological properties of layers III and IV will be interpreted later for all the profiles.

Resistivity Cross Sections

To clarify the effect of lineaments on the resistivity distribution, cross sections of resistivity were constructed along each profile by interpolating the 1-D resistivity models at each site. Arrows in the TEM profiles of Figures 9, 10, and 12–15 indicate the possible fracture positions inferred from the lineaments. The cross sections are divided into layers I to IV, but their distributions are horizontally discontinuous, as is most clearly seen in layers II (≥ 400 Ωm) and III (10–300 Ωm), with layer III becoming much thicker around the fracture zones. In contrast, layer I (4–12 Ωm) generally appears near the surface in all the profiles.

The strike-slip fault type was estimated for the long NW–SE lineaments across profiles 3 and 4 (Figs. 4 and 6). The influences of these faults are confirmed by the clear appearance of layer III adjacent to them (Fig. 9). In addition, the wells near the two profiles and along the fault extension have high potential groundwater yields (Fig. 6). This implies that large amounts of groundwater are stored in the pores of fractured and weathered layer III. Other relatively low ρ zones in layer III under sites ULO 34 and ULO 35, apart from the fracture zone, mark the transition from quartz-feldspar and amphibolitic gneiss to the main rock type—the biotite hornblende quartz-feldspar banded gneiss.

Profile 11 traverses a reverse fault type in the metasedimentary formation, and the effect of the fracture zone is not evident in the resistivity cross section. Layer II, a highly resistive layer, is thick throughout this profile with a typical thickness of 50 m, reaching a maximum of 80 m in the vicinity of the assumed fracture zone (Fig. 10), while layer III is not present at the fractured zone. The absence of layer III is correlated with the moderate potential

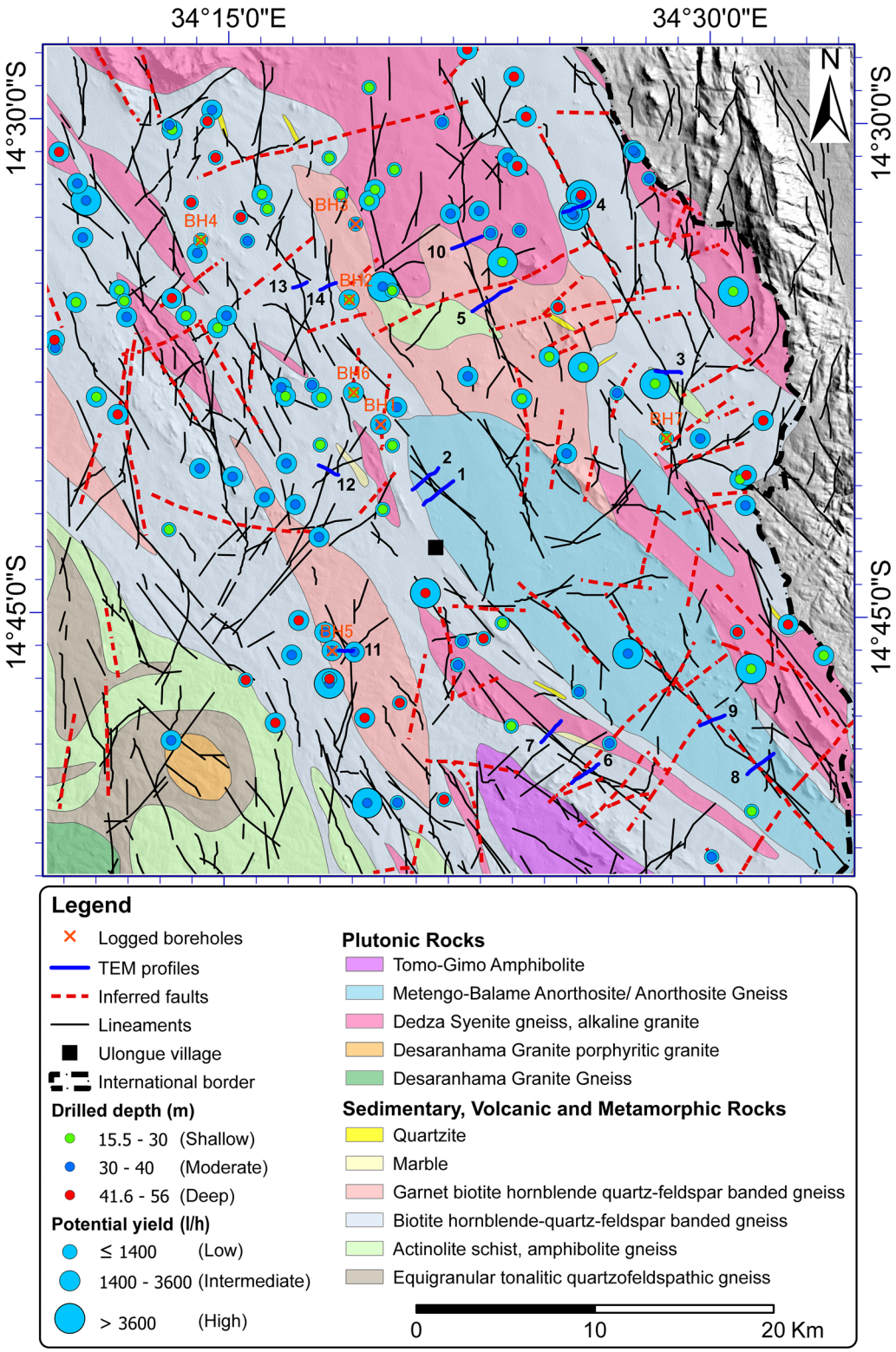

Figure 6. Location of 14 TEM profiles across the lineaments overlaid on the geological map with a SRTM DEM shaded relief backdrop. Well data were supplied by the Water and Sanitation Division of Tete Province (DAS-Tete).

Table 2. Interpreted fault type of grouped lineaments (Fig. 4) and rock type for TEM profile traverses

TEM profiles	Fault type	Rock type	Cross section
1 and 2	Normal	Plutonic	Figure 12
8 and 9	Reverse[a]	Plutonic	Figure 12
11	Reverse	Sedimentary and metamorphic	Figure 10
4	Strike-slip[a]	Sedimentary and metamorphic	Figure 9
3, 5, 6 and 12	Strike-slip	Sedimentary and metamorphic	Figures 9, 13, 14, and 15
7 and 10	Strike-slip	Transition between metamorphic and plutonic	Figures 13 and 14
13 and 14	No fault	Sedimentary and metamorphic	Figure 15

Profile numbers are shown in Figure 6. Figure numbers of resistivity cross sections along the profiles are also listed to show the relationship between the profile pairs traversing the same lineament or distinct lineaments in the same rock type

[a] Lineament overlapped with an inferred fault shown on the geological map

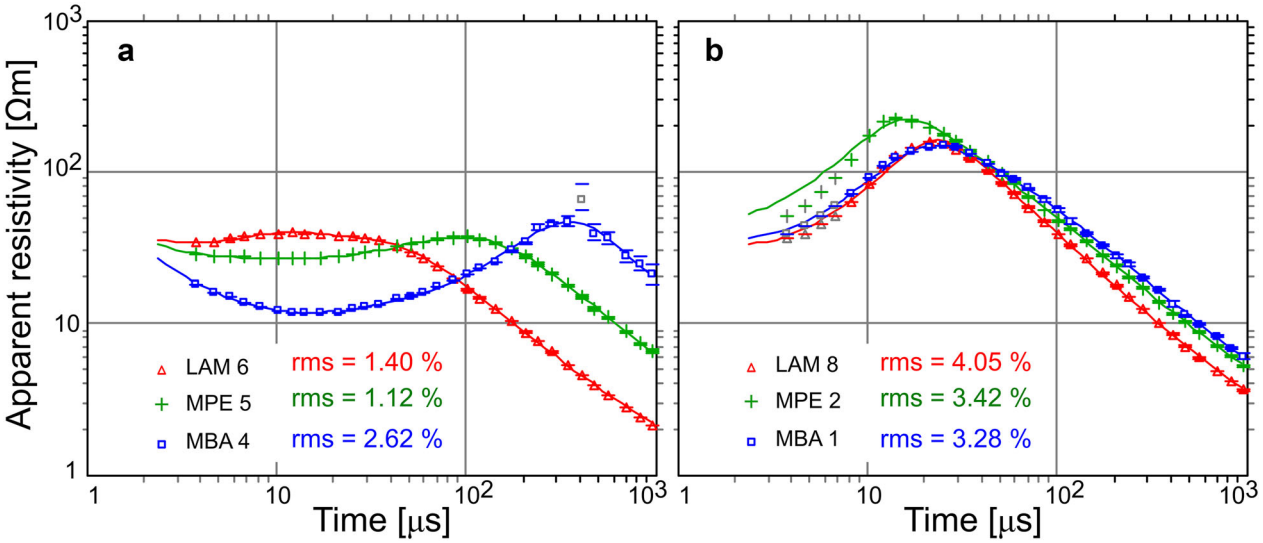

Figure 7. Examples of representative TEM apparent resistivity data and resistivity curves using the resistivity values calculated by the inversion at sounding sites (**a**) inside and (**b**) outside the lineament zones. Rock types: sedimentary for the sounding sites LAM 6 and LAM 8 on profile 12; transitional between metamorphic and plutonic for MPE 2 and MPE 5 on profile 10; and plutonic for MBA 1 and MBA 4 on profile 8.

yield of the 40-m-deep groundwater wells near this profile (Fig. 6). The absence of layer III near the fracture zone might be related to the properties of the reverse fault, such as wide development of a gouge zone that blocks the groundwater flow.

Based on information from a 1:1,000,000 scale hydrogeological map (DNA 1987), it can be deduced that profiles 1, 2, 8, and 9 contain aquifers in the Metengo-Balame anorthosite gneiss, which are characterized by moderate productivity (Fig. 11). The moderately conductive layer classified as layer III is the most obvious and thick layer around the fracture zone in the resistivity cross section along profile 8 (Fig. 12c). This is similar to the effects depicted in profiles 3 and 4 (Fig. 9). Although profiles 1 and 2 are located in the same rock type and in similar topographic features as profile 8 (Table 2), the effect of the fracture zones is not evident (Fig. 12a and b). Outcrops of weathered gneiss and duricrust were dominant at the ground surfaces in profiles 1 and 2, and continuous increases in the ρ_a curves and large noise levels appeared in the late times of the decaying voltage at the sites on these profiles. This suggests the presence of highly resistive media. One noteworthy feature is the wide distribution of the highly conductive layer IV in the deep parts (Fig. 12c), in a similar fashion to the cross section of profile 9, located 3.6 km distance north-

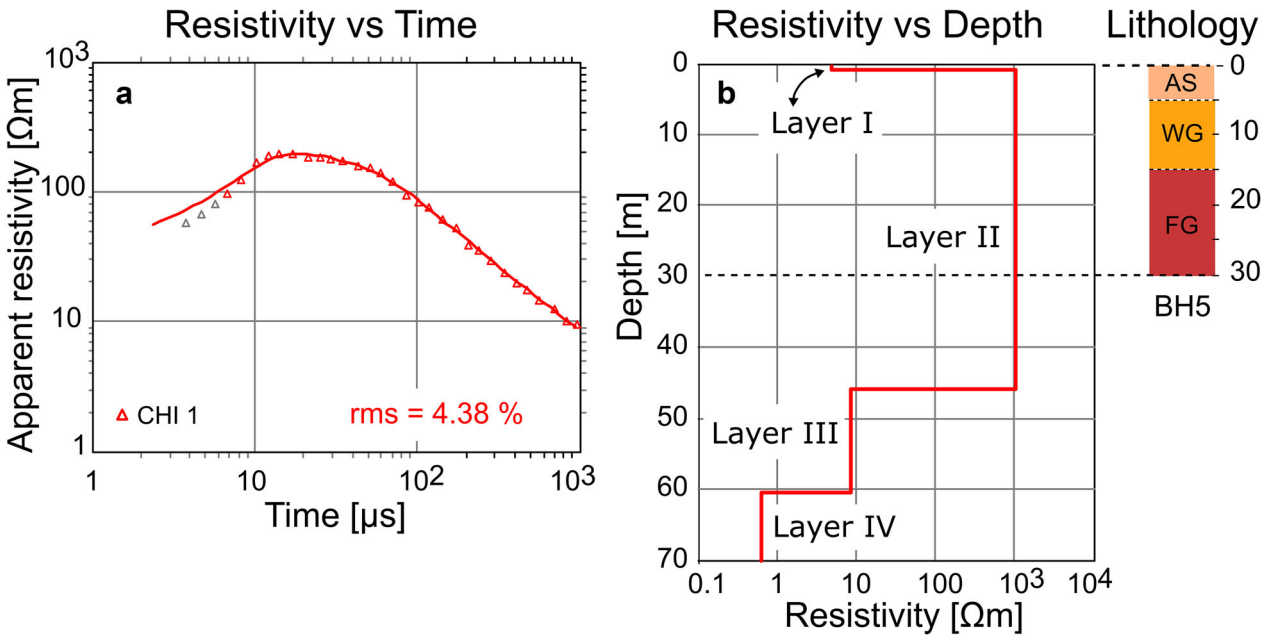

Figure 8. (**a**) Apparent resistivity data and resistivity curve using the resistivity calculated by the inversion at site CHI 1 on profile 11, and (**b**) resistivity model composed of four layers compared with a geological column model for site BH5. Lithological codes AS, WG, and FG refer to alternating sediments, weathered gneiss, and fractured gneiss, respectively. Hydrogeological interpretations of these layers are provided later in the text.

west of profile 8 (Fig. 12d). The same lineament is intercepted by profiles 8 and 9 (Figs. 4 and 6). This vertical feature, with low ρ values, may reflect the irregular basement shape. The similarity in resistivity structures found in two neighboring profiles (profiles 1 and 2) testify to the reliability of the TEM resistivities for interpreting subsurface structures.

A profile pair (6 and 7) in the same direction, but 3 km apart, was selected to investigate the effects of the fracture zone formed by the same lineament. Layer III is clearly evident and a low ρ zone extends widely around the fracture in profile 6 (Fig. 13a). Although this phenomenon is not found in profile 7, layer III appears in the 20 to 40 m depth range between sites ULO 72 and 75 (Fig. 13b). This depth range corresponds to the transition zone from metamorphic to plutonic rocks (Fig. 6). The wide extent of layer IV in the deep zone is common to both profiles and could be caused by the presence of clay minerals, iron oxides, and/or graphite in the marble formation beneath the plutonic rock (Fig. 6).

Profiles 5 and 10 are situated in the same rock type. These profiles were used to investigate the effects of the River Mawe, which is the longest river in the study area and flows strongly, even in the dry season. The River Mawe flows along a fracture zone. In profile 10, layer III clearly appears around the fracture zone, thickens a little at the ENE side of the River Mawe, and reaches its maximum at the transition zone between the metasedimentary and plutonic rocks around MPE 6 and MPE 8 (Figs. 6 and 14a). This transition zone is also marked by layer III in profile 7. The River Mawe is located around ULO 50 in profile 5, and a valley plain extends for a great distance in the northeast direction. A low ρ zone (ranging from 3 to 16 Ωm) continues in the top layer of the plain with a thickness of 1 to 19 m (Fig. 14b). In this profile, layer III appears around ULO 51 only at the southwestern edge where the quartz-feldspar amphibolitic gneiss is distributed. Unlike profile 10, profile 5 is governed by large thicknesses with high ρ values, and layer III does not appear around the fracture zone and the River Mawe. Because gneiss outcrops around ULO 48 and 49, the degree of weathering and fracturing of the bedrocks is considered to be small in profile 5, and this can decrease the water content.

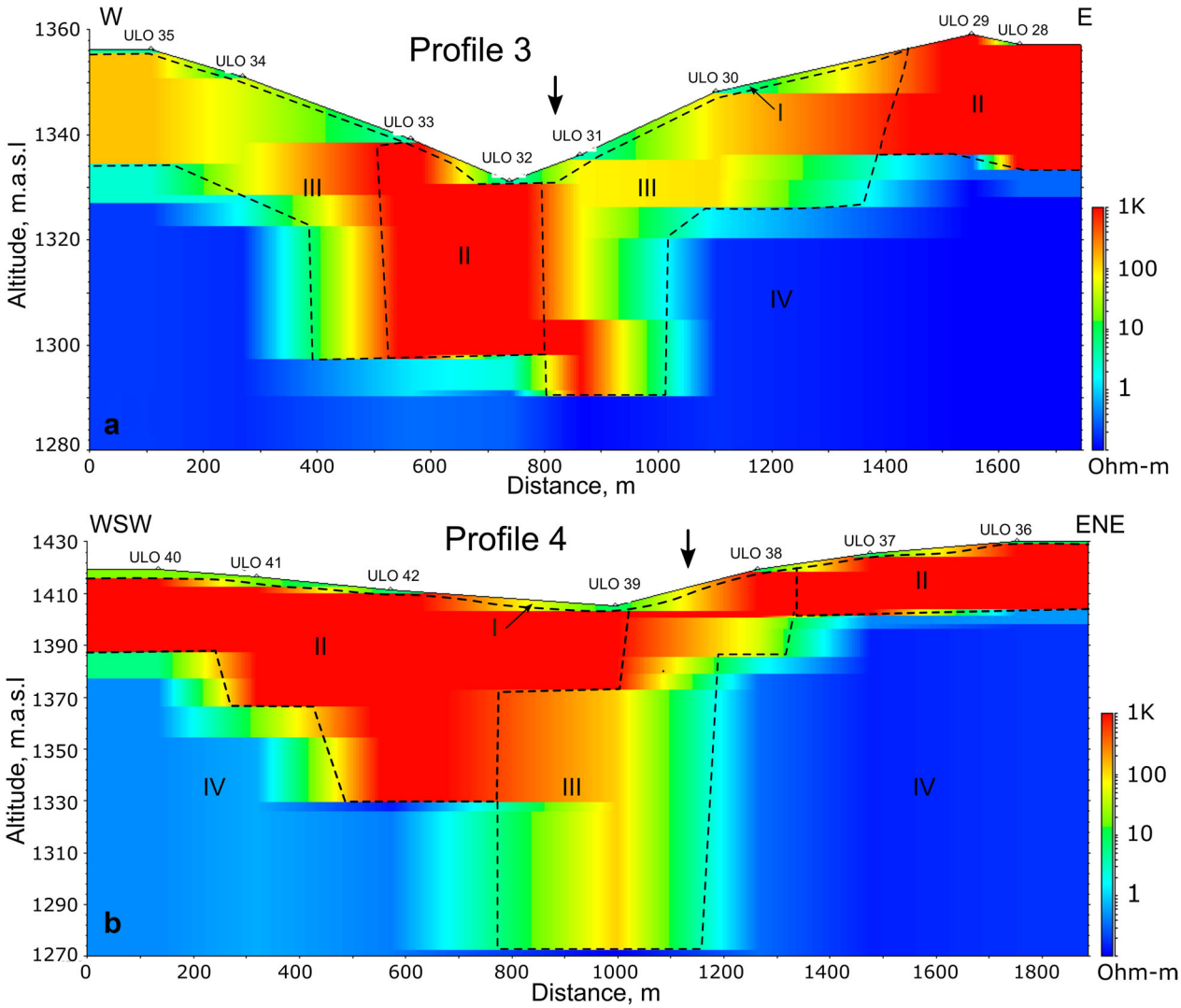

Figure 9. 2-D resistivity cross sections along profiles 3 and 4 (Fig. 6), divided into four resistivity layers (I to IV), depending on the magnitude of resistivity values. Arrows indicate the possible positions of fractures inferred from the lineaments in Figure 6. The descriptions referring to the four layers and arrows also apply to Figures 10, and 12–15.

Finally, a profile pair (13 and 14), and profile 12, were selected to verify the effects of short lineaments from which the fault type was not estimated, and the effects of lineament intersections on resistivity. Profiles 13 and 14 were taken across two parallel lineaments 1.6 km apart (Fig. 6) in metasedimentary rocks. The two resistivity cross sections have different characteristics (Fig. 15a and b). Although layer III appears around the lineament zone in profile 14, layer III is located away from the lineament zone in profile 13, and layer II predominates the lineament zone around site MAD 5. In profile 12, a profile in the same rock type, two lineaments cross to form an X-shape (Fig. 6), and layer III can be discriminated clearly (Fig. 15c) around the lineaments. This suggests a wide extent of the

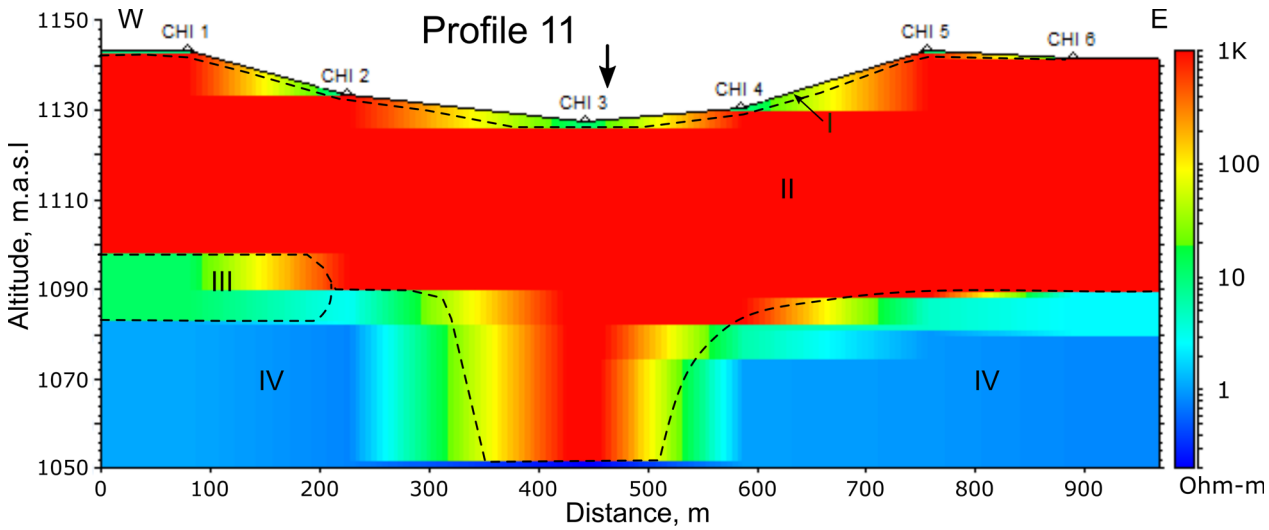

Figure 10. 2-D resistivity cross section along profile 11, which crosses a lineament along a reverse fault type—the only reverse fault encountered in the 14 profiles.

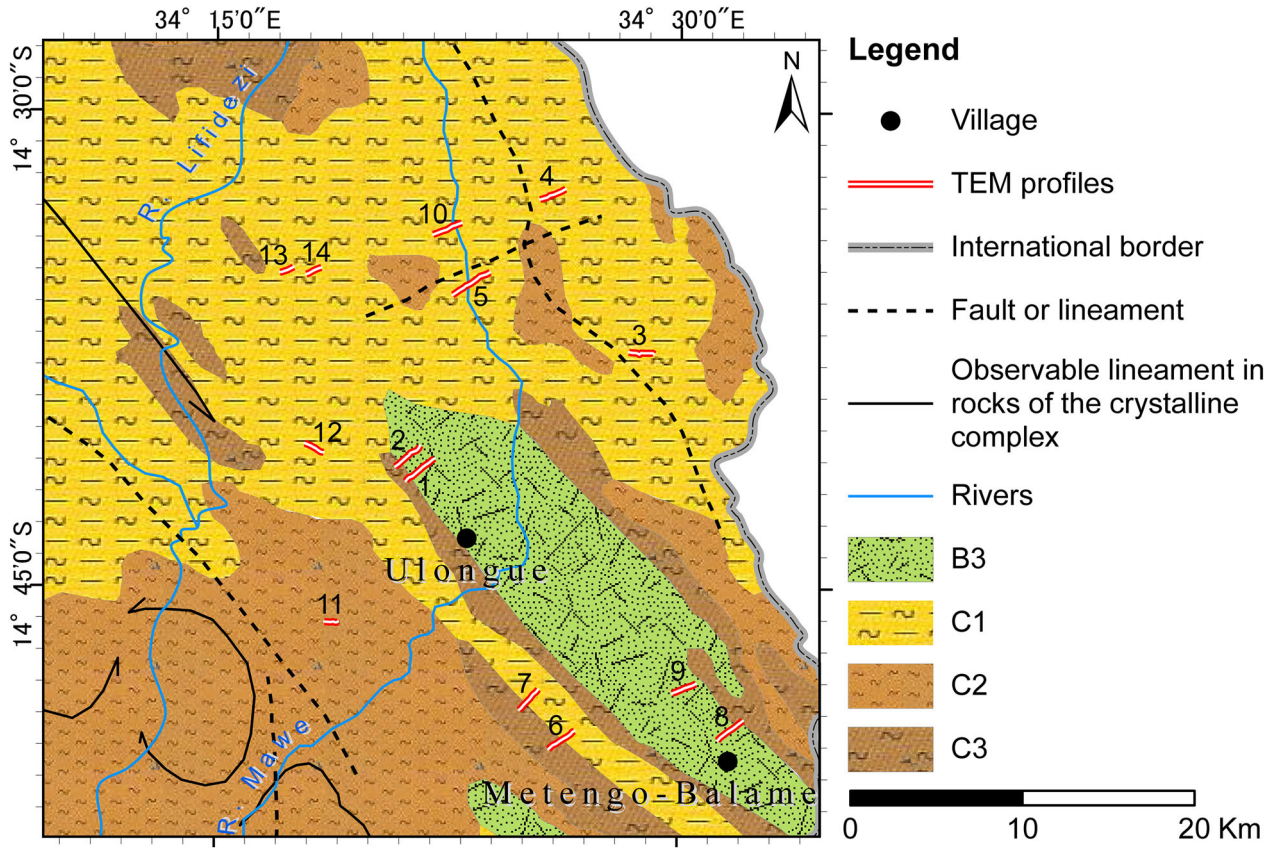

Figure 11. Hydrogeological map of the study area modified after DNA (1987) and overlain by the TEM profiles. B3: predominantly fractured aquifers with moderate productivity and low permeability, C1: areas of continuous or discontinuous local aquifers with limited productivity and low to very low permeability, C2: areas of limited groundwater occurrence with very low permeability, and C3: mountainous areas practically devoid of groundwater with very low to zero permeability.

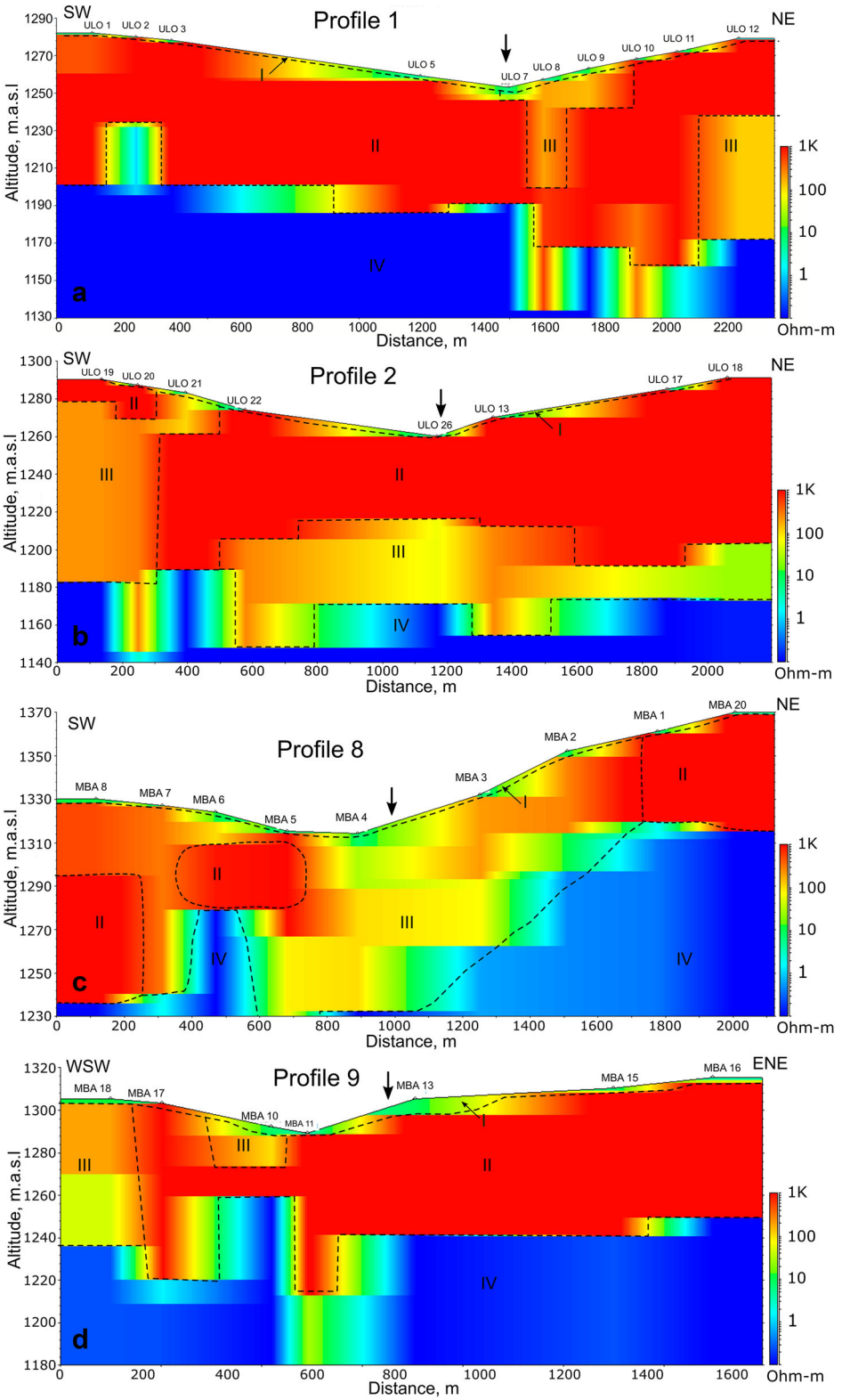

Figure 12. 2-D resistivity cross sections along profiles 1, 2, 8, and 9 across aquifers in the Metengo-Balame anorthosite gneiss. Profiles 1 and 2, and 8 and 9 are in close proximity and form pairs.

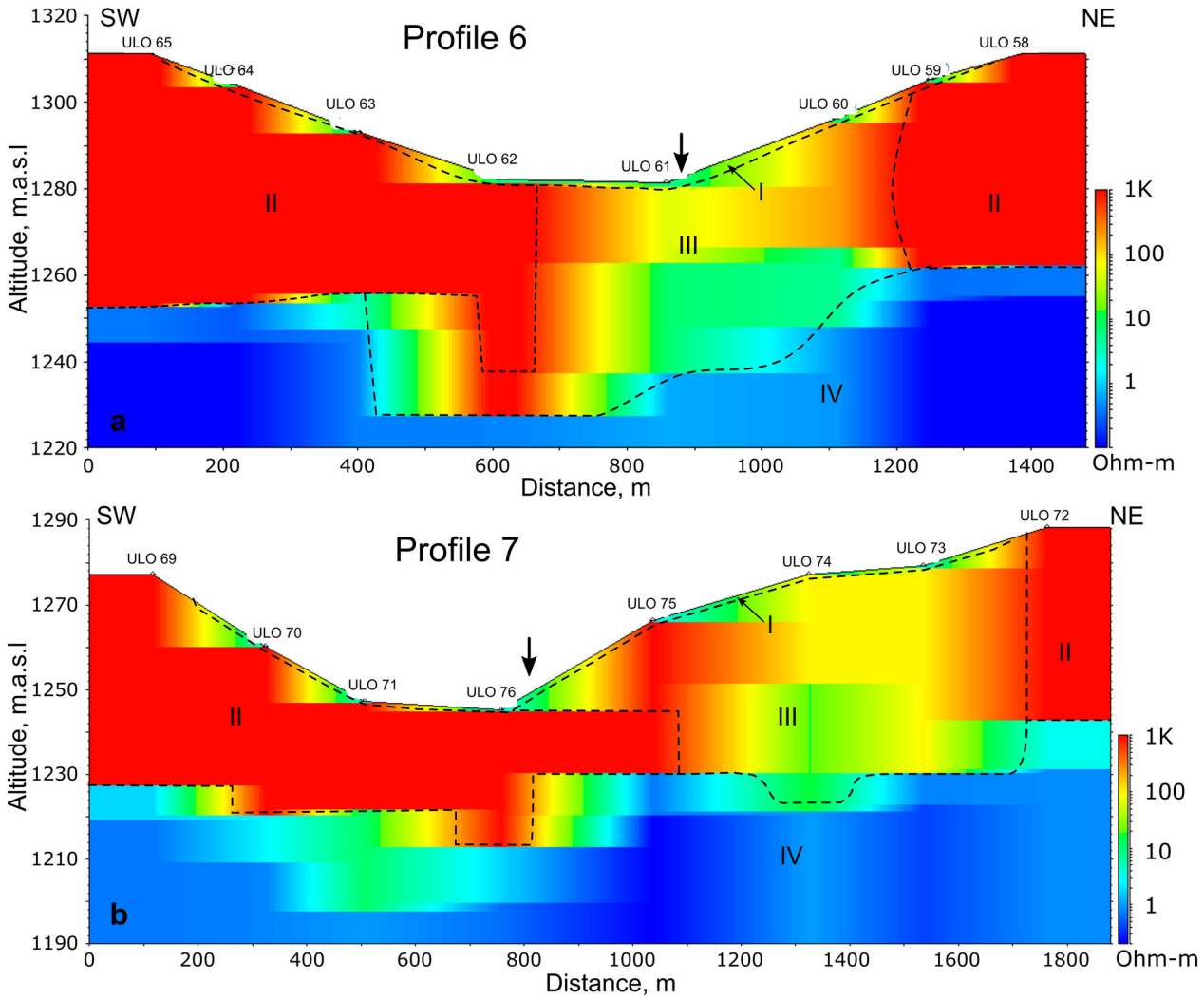

Figure 13. 2-D resistivity cross sections along profiles 6 and 7 across a predicted fracture zone formed by the same lineament (Fig. 6).

fractured zone. Therefore, the presence of lineaments, even if they are short, apparently facilitated weathering of layer III.

DISCUSSION

Geological Interpretation of the Resistivity Layers

The conductive layer IV with $\rho < 10\ \Omega$m was common to all the resistivity cross sections. Considering the geology of the study area, it is postulated that the most plausible explanation for this feature is the presence of graphite or secondary clay minerals in the weathered and fractured zones in the bedrock. This interpretation is supported by the occurrence of several clay and graphite deposits in marble, veinlets, and fracture fills in the anorthosites and in some gneisses surrounding the anorthosite in the study area (Lächelt 2004; CGS 2007).

Around fracture zones inferred from the locations of the lineaments, layer III (moderately conductive) was found to be widespread and thick below layer I except in profiles 2, 5, 9, and 11. The distribution of layer III could be the result of water-saturated formations with moderate porosity and permeability, as suggested by Acworth (1987). Layer II (resistive) extends predominantly outside the fracture zones from the surface when layer I is absent, as shown in Figures 9, 10, 12, 13, 14, and 15.

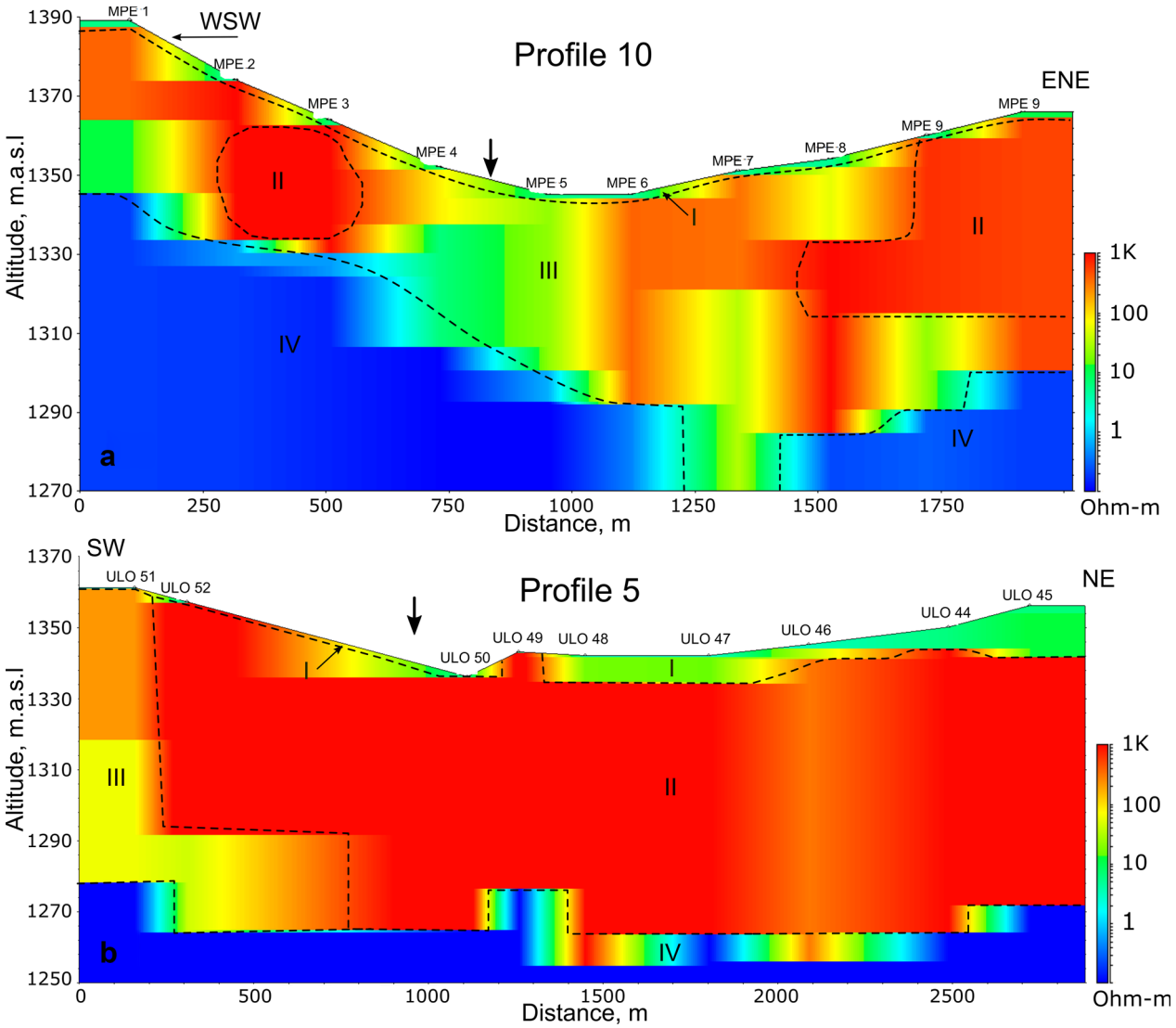

Figure 14. 2-D resistivity cross sections along profiles 5 and 10 across the River Mawe, which is inferred to flow on the fracture zone.

The surface materials are chiefly composed of alternating sediments such as loose red sandy soil and dark loamy soils. These sediments are permeable and form a recharge zone for the underlying aquifers. The general landscape and surface materials common to all profile areas are shown in Figure 16. Because layer II has high ρ, its water content and porosity may be small at shallow depths and in the basement, respectively.

In addition to water content, TEM resistivity is sensitive to conductive materials such as clay and sulfide minerals. Fracturing and faulting largely influence the permeability of the weathered layer because they can enhance the permeability, whereas fault gouge and secondary clay minerals formed by weathering significantly reduce the permeability (Acworth 1987; Bense et al. 2013). As result, saturated and unsaturated zones cannot be distinguished solely by resistivity (Auken et al. 2006).

Assessment of Groundwater Potential

To further advance the interpretation of the TEM resistivity distribution and its correlation with the amount of stored groundwater, a groundwater potential (*GWP*) map was produced using ArcGIS that integrated easily available topographic features

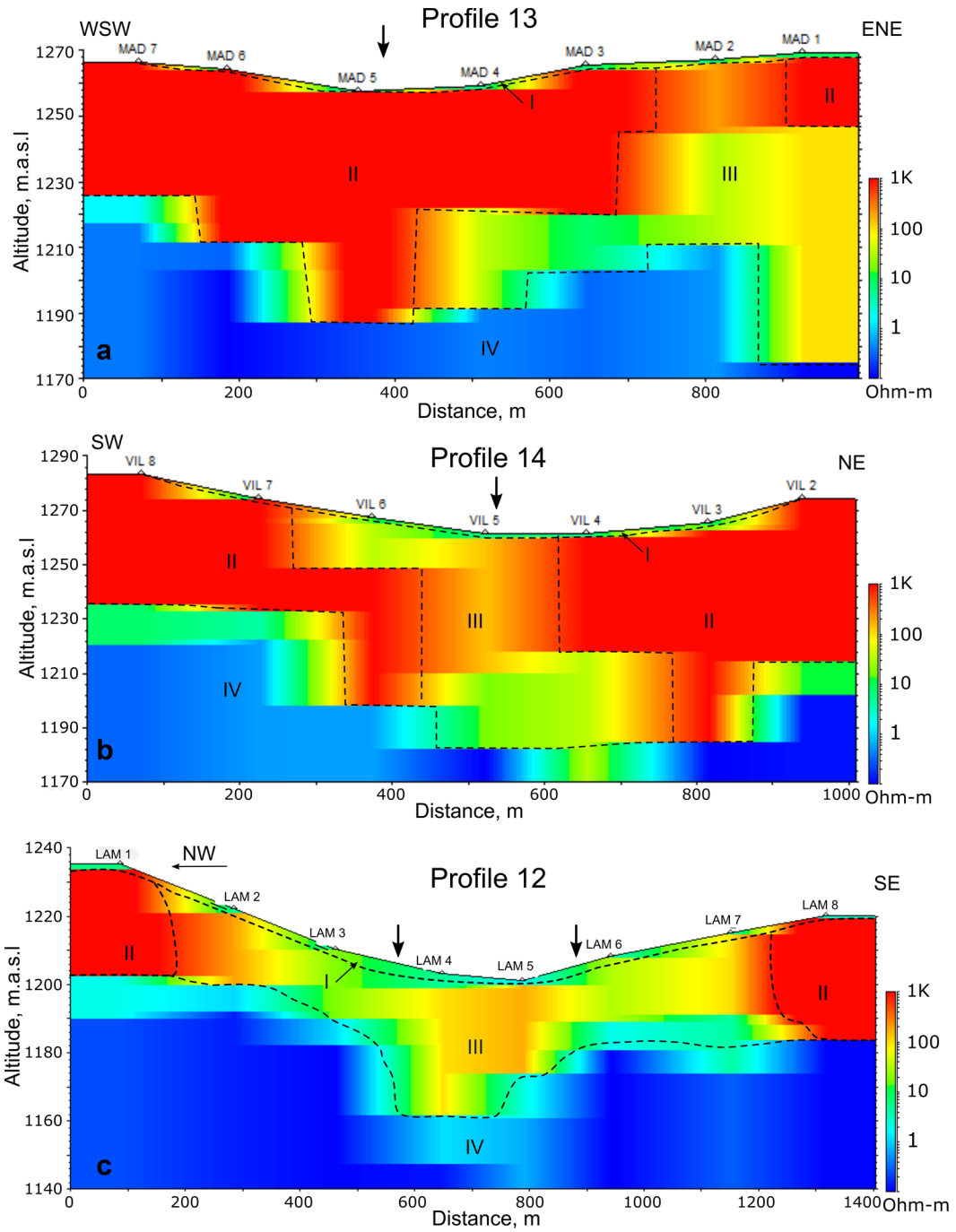

Figure 15. 2-D resistivity cross sections along profiles 12, 13, and 14 in metasedimentary rocks. Profile pair (13 and 14), and profile 12, transverse two short parallel lineaments and two crossing lineaments forming an X-shape, respectively (Fig. 6).

(slope angle), lineament density and ancillary data (vegetation index and proximity to lineament), and geology (Fig. 2). This map can be used to increase the success ratio of installing groundwater wells. *GWP* is based on a traditional weighted sum technique using the reclassified thematic maps:

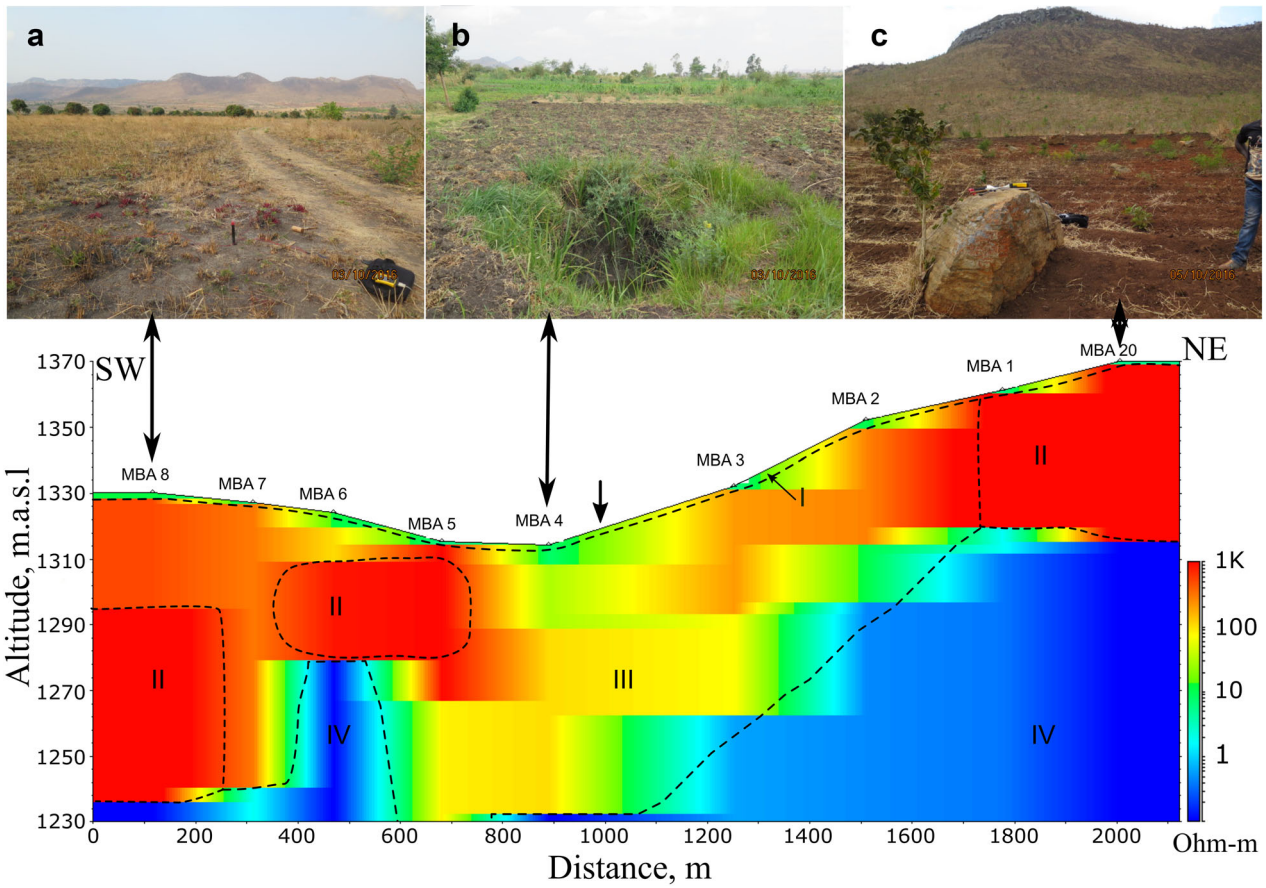

Figure 16. Photographs taken from profile 8 facing toward the NE (the resistivity cross section) showing the general landscape and surface materials common to all the profiles (Fig. 12c): (**a**) site MBA 8 with a hard, dark, clayey surface, and stressed vegetation; (**b**) dug well of 1.3 m depth for irrigation at site MBA 4 inside the lineament zone with very dark clayey soil and green vegetation; and (**c**) loose, red, sandy soil with high resistivity at site MBA 20.

$$GWP = \sum w_i R_i \tag{6}$$

where w_i is the weight value for each map and R_i is the rating of each map class. Because there are five thematic maps, the average weight is 20%. The weights were determined by considering the influence of each thematic map, avoiding overweighting or underweighting, and comparing the resultant *GWP* with the referenced flow data at the wells. This method is commonly used in GIS-based groundwater potential studies (e.g., Krishnamurthy et al. 1996; Shahid et al. 2000). As a result, 10, 5, 0, − 5, and − 10% were added to the strong, relatively strong, medium, relatively weak, and weak influences, respectively, which were equal to 1.5, 1.25, 1, 0.75, and 0.5 times the average value. Following this rule, the weights assigned were 30% for lineament density, 25% for slope angle, 20% for geology, 15% for MSAVI, and 10% for proximity to lineaments. Consequently, the map classes were assigned different categories based on their contributions to groundwater recharge, with a rating from 1 to 4, where classes 1 and 4 represented the least and greatest contributions, respectively.

The largest weight assigned to lineament density was based on TEM resistivity indications of the fracture control of groundwater potential in the crystalline basement rocks. In addition, the strong control of slope on runoff and infiltration is known (Abdalla 2012); the infiltration rate of rainfall decreases as the slope angle increases (Fox et al. 1997). Because they are highly fractured, the Metengo-Balame anorthosite and anorthosite gneiss rocks were demarcated as moderately productive aquifers

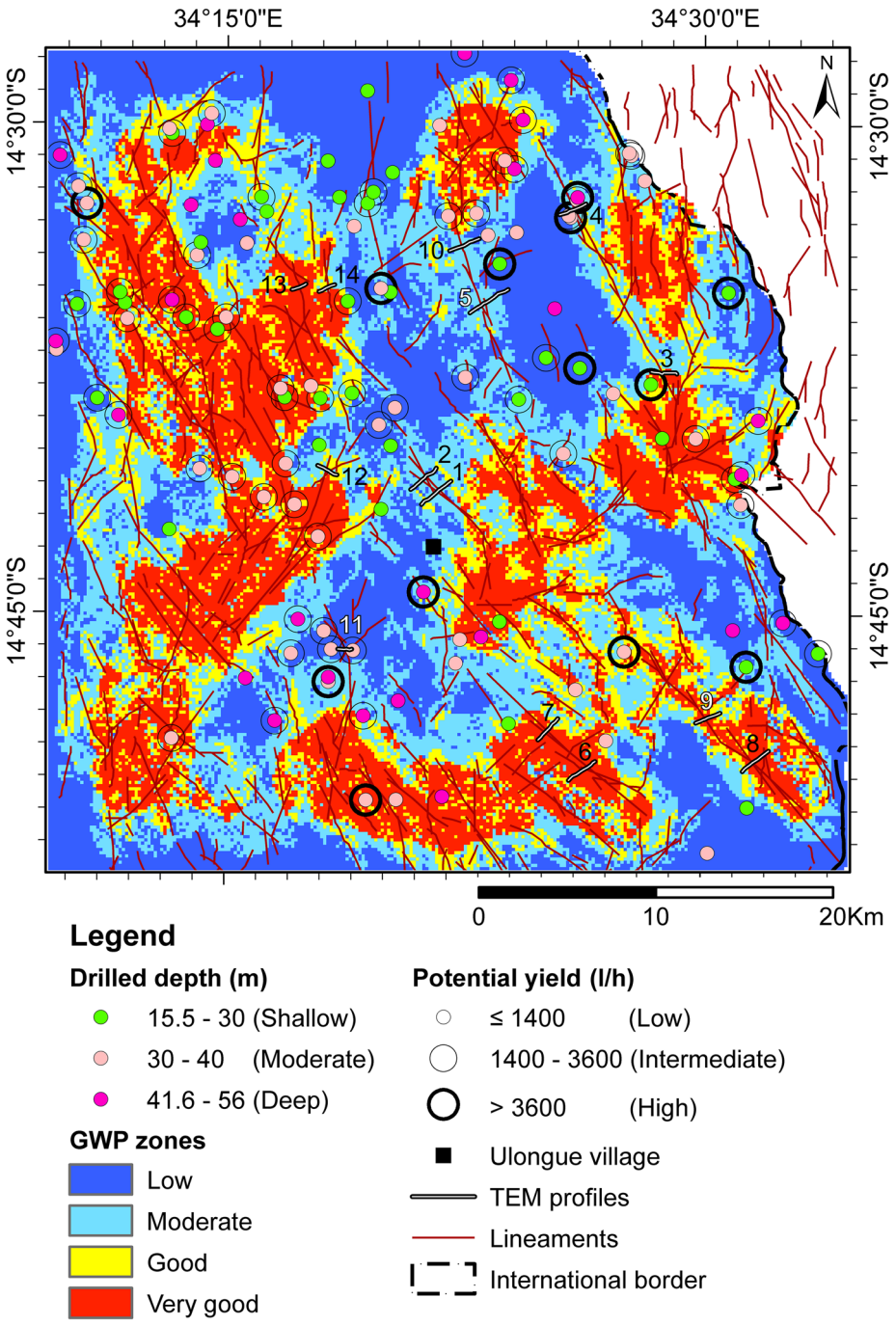

Figure 17. Groundwater potential map produced from the integration of five factors: lineament density, proximity to lineament, slope angle, vegetation index, and geology. Profile numbers colored white signify the profiles with absence of layer III around the lineament zone. Well locations are overlaid on the map to examine the correspondence between the groundwater potential yield and *GWP* levels.

on the hydrogeological map of the area (Fig. 11) (DNA 1987). Therefore, a high rating value was assigned to these rocks. As mentioned above, the presence of groundwater at shallow depths can be inferred from high vegetation indices (MSAVI in this study) in the dry areas and seasons. The high

Table 3. Relationship between *GWP* category and presence of layer III around the lineament zone for each profile

TEM resistivity profile	Presence of layer III around fracture zone	*GWP* category
1	Present	Moderate
2	Below layer II	Low
3	Present	Very good
4	Present	Moderate
5	Absent	Moderate
6	Present	Very good
7	Present	Very good
8	Present	Very good
9	Absent	Very good
10	Present	Moderate
11	Absent	Low
12	Present	Good
13	Below layer II	Very good
14	Present	Good

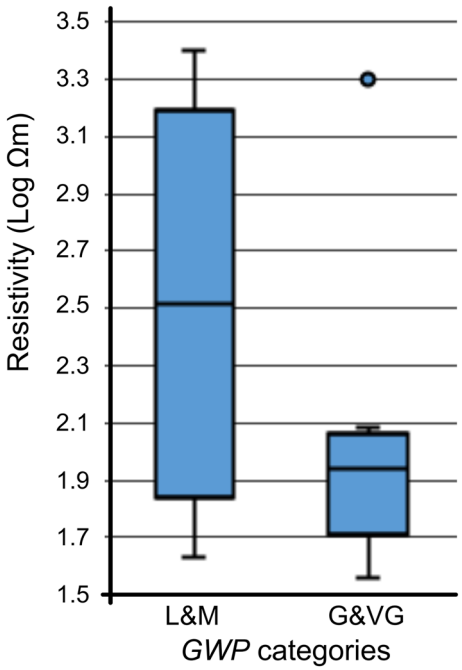

Figure 18. Correlation of average resistivity values of layer III around the lineaments and the *GWP* categories for the 14 profiles using box plots. The average resistivity of layer II around the lineament was used for the profiles where layer III was absent.

vegetation indices also originated from the development of fractures. Therefore, proximity to lineaments (buffer zone) was considered in addition to MSAVI.

To facilitate interpretation, *GWP* was classified into four categories: low (L) = less than the lower quartile of the resultant *GWP* value; moderate (M) = from the lower quartile to the median; good (G) = from the median to the upper quartile; and very good (VG) = higher than the upper quartile. Area proportions of these categories over the study area were L: 31.3%, M: 30.4%, G: 15%, and VG: 23.3%. The final *GWP* map (Fig. 17) reveals that the L category zones are concentrated in high elevations, from which rainwater runoff predominates because of the steep slopes. The M category zones are mainly associated with low lineament density and less green vegetation areas. The G category zones occur at the transition between the M and VG categories. The G and VG category zones are distributed in areas with high densities of lineaments, as well as around the dominant lineaments. These areas are related to highly weathered zones inferred from the TEM cross sections and are also marked by gentle slopes and active vegetation.

Additionally, the well locations were added to the *GWP* map to verify it. There is no clear correlation between well depth and groundwater potential yield because of the complex nature of crystalline basement aquifers. However, 79% of the 43 wells with low potential yield ($\leq$ 1400 l/h) are located in low to moderate *GWP* zones, and 42% of the 75 wells classified as intermediate to high potential yield (> 1400 l/h) are located in the good to very good *GWP* zones. These proportions cannot be used exclusively to evaluate the *GWP* map accuracy because the number and distribution of the wells are limited. For example, there are only two wells in the fractured aquifers of the Metengo-Balame anorthosite/anorthosite gneiss (B3 in the hydrogeological map in Fig. 11). However, the correspondence between the levels of groundwater potential yield and *GWP* zones indicates that the derived proportions generally support the effectiveness of the *GWP* map.

Next, the *GWP* map was correlated with the presence or absence of the most important aquifer indicator resistivity layer (layer III) in the vicinity of the lineament zone, and the results are summarized in Table 3. Good correlation was shown among profiles 1, 4, and 10, profiles 12 and 14, and profiles 3, 6, 7, and 8, which contained layer III and are located in the M, G, and VG categories, respectively. In contrast, profiles 5 and 11, with no signature of layer III, are in the M and L categories, respectively. Although profiles 9 and 13 are located in the VG cat-

egory, layer III is absent or appears below layer II. As an empirical measure, the average ρ values of layer III around the lineaments were related to the *GWP* categories using box plots for the 14 profiles (Fig. 18). The average ρ of layer II around the lineaments was used in the plots for the profiles where layer III is absent (i.e., profiles 2, 5, 9, and 11). Because the number of profiles is limited, the four *GPW* categories were grouped into upper potential (VG and G) and lower potential (M and L). The plots reveal that the average ρ values are generally lower in the VG and G categories than in the L and M categories, except for an outlier that originated from layer II in profile 9. Therefore, the *GWP* categories can be well correlated to resistivity characteristics around the fractures with respect to the aquifer formation. This confirms the reliability of the *GWP* map and the applicability of the lineament, topography, geology, and vegetation activity information for groundwater resource assessment in Precambrian crystalline rock areas.

CONCLUSIONS

This study aimed to assess groundwater potential and to identify high potential zones in a Precambrian crystalline rock area without a detailed drilling dataset of hydrogeological and hydraulic properties. This was done by combining lineament extraction from multi-shaded digital elevation model, a vegetation index from optical sensor images, and a transient electromagnetic survey. An area of 45 km $\times$ 45 km covered by crystalline basement in central western Mozambique was selected for the case study. The fracture distributions were estimated by lineament extraction using the segment tracing algorithm, and three predominant trends along NNW, NE, and NNE were found to follow the inferred faults on a geological map. Rough flow rate data at 118 wells, and vegetation indices obtained from two Landsat 8 OLI images of a dry and rainy season, were used as ancillary information for the shallowness and amount of stored groundwater. The potential yields of groundwater tended to increase in the proximity of lineaments, and the greenness of vegetation in the dry season was found to be constant along the lineaments. Therefore, the lineaments extracted are probably related to fracture zones that could be paths for groundwater flow in the shallow zones and aquifers.

The transient electromagnetic resistivity cross sections along the 14 profiles were selected across long lineaments that straddled several rock types. The most noteworthy feature was the appearance of a moderate resistivity zone with a large thickness around the lineaments from the surface to large depths. The occurrence of this moderate resistivity zone changed with location. This resistivity zone also appeared in the transition zones between two lithological units. However, heterogeneity in the degrees of weathering and fracturing was inferred because the resistivities were high, as a whole, in some profiles.

A groundwater potential map was produced by integrating five water-related factors: lineament density, slope, geology, vegetation index, and proximity to lineament. Very good potential zones were identified in areas of dense lineaments and around long lineaments related to fractures. However, the shallow aquifers have low potential even near the fracture zones because of the presence of a thick resistive layer over the moderately conductive layer near the fracture zones.

The combination of topographic and vegetation greenness analyses, and near surface resistivity modeling, were demonstrated to be effective for detecting fracture zones and evaluating groundwater potential. This rapid and cost-effective technique can be widely applied to tropical savannas covered by crystalline basements that lack detailed drilling surveys, as in this study.

ACKNOWLEDGMENTS

The authors would like to express their gratitude to the Japan International Cooperation Agency (JICA) for funding the field survey and supporting this research. We thank the Water and Sanitation Division (Direcção de Água e Saneamento) of Tete Province in Mozambique, for providing the wells data. Sincere thanks are extended to the two anonymous reviewers for their valuable comments and suggestions that helped improve the clarity of the manuscript.

REFERENCES

Abdalla, F. (2012). Mapping of groundwater prospective zones using remote sensing and GIS techniques: A case study from the Central Eastern Desert, Egypt. *Journal of African Earth Sciences, 70,* 8–17. https://doi.org/10.1016/j.jafrearsci.2012.05.003.

Acworth, R. I. (1987). The development of crystalline basement aquifers in a tropical environment. *Quarterly Journal of Engineering Geology and Hydrogeology, 20*(4), 265–272. https://doi.org/10.1144/GSL.QJEG.1987.020.04.02.

Archie, G. E. (1942). The electrical resistivity log as an aid in determining some reservoir characteristics. *Transactions of the AIME, 146*(1), 54–62. https://doi.org/10.2118/942054-G.

Árnason, K. (1989). *Central loop transient electromagnetic soundings over a horizontally layered earth*. Reykjavik: OS-89032/JHD-06.

Auken, E., Pellerin, L., Christensen, N. B., & Sørensen, K. (2006). A survey of current trends in near-surface electrical and electromagnetic methods. *Geophysics, 71*(5), G249–G260. https://doi.org/10.1190/1.2335575.

Barsukov, P. O., Fainberg, E. B., & Khabensky, E. O. (2006). Shallow investigations by TEM-FAST technique: methodology and examples. *Methods in Geochemistry and Geophysics, 40,* 55–77. https://doi.org/10.1016/S0076-6895(06)40003-2.

Bense, V. F., Gleeson, T., Loveless, S. E., Bour, O., & Scibek, J. (2013). Fault zone hydrogeology. *Earth-Science Reviews, 127,* 171–192. https://doi.org/10.1016/j.earscirev.2013.09.008.

Bicca, M. M., Philipp, R. P., Jelinek, A. R., Ketzer, J. M. M., dos Santos Scherer, C. M., Jamal, D. L., et al. (2017). Permian-Early Triassic tectonics and stratigraphy of the Karoo Supergroup in northwestern Mozambique. *Journal of African Earth Sciences, 130,* 8–27. https://doi.org/10.1016/j.jafrearsci.2017.03.003.

Brunner, P., Hendricks Franssen, H.-J., Kgotlhang, L., Bauer-Gottwein, P., & Kinzelbach, W. (2007). How can remote sensing contribute in groundwater modeling? *Hydrogeology Journal, 15*(1), 5–18. https://doi.org/10.1007/s10040-006-0127-z.

CGS. (2007). *Map Explanation: Sheets Furancungo (1433) and Ulongue (1434), Scale 1:250000*. Maputo: Ministério dos Recursos Minerais, Direcção Nacional de Geologia.

Chilton, P. J., & Foster, S. S. D. (1995). Hydrogeological characterisation and water-supply potential of basement aquifers in Tropical Africa. *Hydrogeology Journal, 3*(1), 36–49. https://doi.org/10.1007/s100400050061.

Chongo, M., Vest Christiansen, A., Tembo, A., Banda, K. E., Nyambe, I. A., Larsen, F., et al. (2015). Airborne and ground-based transient electromagnetic mapping of groundwater salinity in the Machile-Zambezi Basin, southwestern Zambia. *Near Surface Geophysics, 13,* 383–395. https://doi.org/10.3997/1873-0604.2015024.

Civco, D. L. (1989). Topographic normalization of Landsat Thematic Mapper digital imagery. *Photogrammetric Engineering and Remote Sensing, 55*(9), 1303–1309.

Costabel, S., Siemon, B., Houben, G., & Günther, T. (2017). Geophysical investigation of a freshwater lens on the island of Langeoog, Germany—Insights from combined HEM, TEM and MRS data. *Journal of Applied Geophysics, 136,* 231–245. https://doi.org/10.1016/j.jappgeo.2016.11.007.

Danielsen, J. E., Auken, E., Jørgensen, F., Søndergaard, V., & Sørensen, K. I. (2003). The application of the transient electromagnetic method in hydrogeophysical surveys. *Journal of Applied Geophysics, 53*(4), 181–198. https://doi.org/10.1016/j.jappgeo.2003.08.004.

Danielsen, J. E., Dahlin, T., Owen, R., Mangeya, P., & Auken, E. (2007). Geophysical and hydrogeologic investigation of groundwater in the Karoo stratigraphic sequence at Sawmills in northern Matabeleland, Zimbabwe: A case history. *Hydrogeology Journal, 15*(5), 945–960. https://doi.org/10.1007/s10040-007-0191-z.

DNA. (1987). *Carta Hidrogeológica escala 1:1000000, 1ª edição*. Maputo: Ministério de Construção e Águas, Direcção Nacional de Águas.

DNG. (2006). *Geological sheet 1:250000, No. 1434*. Maputo: Ministério dos Recursos Minerais, Direcção Nacional de Geologia.

Fitterman, D. V., & Stewart, M. T. (1986). Transient electromagnetic sounding for groundwater. *Geophysics, 51*(4), 995–1005.

Fox, D. M., Bryan, R. B., & Price, A. G. (1997). The influence of slope angle on final infiltration rate for interrill conditions. *Geoderma, 80*(1–2), 181–194. https://doi.org/10.1016/S0016-7061(97)00075-X.

Henebry, G. M. (1993). Detecting change in grasslands using measures of spatial dependence with landsat TM data. *Remote Sensing of Environment, 46*(2), 223–234. https://doi.org/10.1016/0034-4257(93)90097-H.

Jarvis, A., Reuter, H. I., Nelson, A., & Guevara, E. (2008). *Hole-filled SRTM for the globe Version 4,* available from the CGIAR-CSI SRTM 90m Database. http://srtm.csi.cgiar.org. Accessed 11 Sep 2015.

Koike, K., Nagano, S., & Kawaba, K. (1998). Construction and analysis of interpreted fracture planes through combination of satellite-image derived lineaments and digital elevation model data. *Computers & Geosciences, 24*(6), 573–583. https://doi.org/10.1016/S0098-3004(98)00021-1.

Koike, K., Nagano, S., & Ohmi, M. (1995). Lineament analysis of satellite images using a Segment Tracing Algorithm (STA). *Computers & Geosciences, 21*(9), 1091–1104. https://doi.org/10.1016/0098-3004(95)00042-7.

Krishnamurthy, J., Venkatesa Kumar, N., Jayaraman, V., & Manivel, M. (1996). An approach to demarcate ground water potential zones through remote sensing and a geographical information system. *International Journal of Remote Sensing, 17*(10), 1867–1884. https://doi.org/10.1080/01431169608948744.

Lächelt, S. (2004). *Geology and mineral resources of Mozambique*. Maputo: Ministério dos Recursos Minerais e Energia, Direcção Nacional de Geologia.

Mallast, U., Gloaguen, R., Geyer, S., Rödiger, T., & Siebert, C. (2011). Derivation of groundwater flow-paths based on semi-automatic extraction of lineaments from remote sensing data. *Hydrology and Earth System Sciences, 15*(8), 2665–2678. https://doi.org/10.5194/hess-15-2665-2011.

Martínez-Moreno, F. J., Monteiro-Santos, F. A., Madeira, J., Bernardo, I., Soares, A., Esteves, M., et al. (2016). Water prospection in volcanic islands by Time Domain Electromagnetic (TDEM) surveying: The case study of the islands of Fogo and Santo Antão in Cape Verde. *Journal of Applied Geophysics, 134,* 226–234. https://doi.org/10.1016/j.jappgeo.2016.09.020.

Masoud, A., & Koike, K. (2006). Tectonic architecture through Landsat-7 ETM+/SRTM DEM-derived lineaments and relationship to the hydrogeologic setting in Siwa region, NW Egypt. *Journal of African Earth Sciences, 45*(4–5), 467–477. https://doi.org/10.1016/j.jafrearsci.2006.04.005.

Masoud, A., & Koike, K. (2011a). Auto-detection and integration of tectonically significant lineaments from SRTM DEM and remotely-sensed geophysical data. *ISPRS Journal of Photogrammetry and Remote Sensing, 66*(6), 818–832. https://doi.org/10.1016/j.isprsjprs.2011.08.003.

Masoud, A., & Koike, K. (2011b). Morphotectonics inferred from the analysis of topographic lineaments auto-detected from DEMs: Application and validation for the Sinai Peninsula, Egypt. *Tectonophysics, 510*(3), 291–308. https://doi.org/10.1016/j.tecto.2011.07.010.

Masoud, A., & Koike, K. (2017). Applicability of computer-aided comprehensive tool (LINDA: LINeament Detection and Analysis) and shaded digital elevation model for characterizing and interpreting morphotectonic features from lineaments. *Computers & Geosciences, 106,* 89–100. https://doi.org/10.1016/j.cageo.2017.06.006.

Matthew, M. W., Adler-Golden, M. S. M., Berk, A., Richtsmeier, S. C., Levine, R. Y., Bernstein, L. S., et al. (2000). Status of atmospheric correction using a MODTRAN4-based algorithm. In S. S. Chen & M. R. Descour (Eds.), *Algorithms for multispectral, hyperspectral, and ultraspectral imagery VI, proceedings of SPIE* (Vol. 4049, p. 207).

Nabighian, M. N. (Ed.). (1991). *Electromagnetic methods in applied geophysics*. Society of Exploration Geophysicists. https://doi.org/10.1190/1.9781560802686.

National Research Council. (1996). *Rock fractures and fluid flow: Contemporary understanding and applications*. Washington, DC: The National Academies Press. https://doi.org/10.17226/2309.

Qi, J., Chehbouni, A., Huete, A. R., Kerr, Y. H., & Sorooshian, S. (1994). A modified soil adjusted vegetation index. *Remote Sensing of Environment, 48*(2), 119–126. https://doi.org/10.1016/0034-4257(94)90134-1.

Ranganai, R. T., & Ebinger, C. J. (2008). Aeromagnetic and Landsat TM structural interpretation for identifying regional groundwater exploration targets, south-central Zimbabwe Craton. *Journal of Applied Geophysics, 65*(2), 73–83. https://doi.org/10.1016/j.jappgeo.2008.05.009.

Reynolds, J. M. (2011). *An introduction to applied and environmental geophysics*. New York: Wiley-Blackwell.

Riaño, D., Chuvieco, E., Salas, J., & Aguado, I. (2003). Assessment of different topographic corrections in landsat-TM data for mapping vegetation types. *IEEE Transactions on Geoscience and Remote Sensing, 41*(5), 1056–1061. https://doi.org/10.1109/TGRS.2003.811693.

Rondeaux, G., Steven, M., & Baret, F. (1996). Optimization of soil-adjusted vegetation indices. *Remote Sensing of Environment, 55*(2), 95–107. https://doi.org/10.1016/0034-4257(95)00186-7.

Rouse, J. W., Haas, R. H., Schell, J. A., Deering, D. W., & Harlan, J. C. (1974). *Monitoring the vernal advancement and retrogradation (green wave effect) of natural vegetation*. Texas: NASA/GSFC, Type II, Progress Report.

Ruland, W. W., Cherry, J. A., & Feenstra, S. (1991). The depth of fractures and active ground-water flow in a clayey till plain in Southwestern Ontario. *Ground Water, 29*(3), 405–417. https://doi.org/10.1111/j.1745-6584.1991.tb00531.x.

Sander, P. (2007). Lineaments in groundwater exploration: A review of applications and limitations. *Hydrogeology Journal, 15,* 71–74. https://doi.org/10.1007/s10040-006-0138-9.

Sapia, V., Viezzoli, A., Jorgensen, F., Oldenborger, G. A., & Marchetti, M. (2014). The impact on geological and hydrogeological mapping results of moving from ground to airborne TEM. *Journal of Environmental and Engineering Geophysics, 19*(1), 53–66. https://doi.org/10.2113/JEEG19.1.53.

Saraf, A. K., & Choudhury, P. R. (1998). Integrated remote sensing and GIS for groundwater exploration and identification of artificial recharge sites. *International Journal of Remote Sensing, 19*(10), 1825–1841. https://doi.org/10.1080/014311698215018.

Shaban, A., Khawlie, M., & Abdallah, C. (2006). Use of remote sensing and GIS to determine recharge potential zones: The case of Occidental Lebanon. *Hydrogeology Journal, 14*(4), 433–443. https://doi.org/10.1007/s10040-005-0437-6.

Shahid, S., Nath, S. K., & Roy, J. (2000). Groundwater potential modelling in a soft rock area using a GIS. *International Journal of Remote Sensing, 21*(9), 1919–1924. https://doi.org/10.1080/014311600209823.

Teillet, P. M., Guindon, B., & Goodenough, D. G. (1982). On the slope-aspect correction of multispectral scanner data. *Canadian Journal of Remote Sensing, 8,* 84–106. https://doi.org/10.1080/07038992.1982.10855028.

Tessema, A., Mengistu, H., Chirenje, E., Abiye, T. A., & Demlie, M. B. (2012). The relationship between lineaments and borehole yield in North West Province, South Africa: results from geophysical studies. *Hydrogeology Journal, 20*(2), 351–368. https://doi.org/10.1007/s10040-011-0803-5.

Wang, L., Tian, B., Masoud, A., & Koike, K. (2013). Relationship between remotely sensed vegetation change and fracture zones induced by the 2008 Wenchuan earthquake, China. *Journal of Earth Science, 24*(2), 282–296. https://doi.org/10.1007/s12583-013-0329-y.

Wright, E. P. (1992). The hydrogeology of crystalline basement aquifers in Africa. *Hydrogeology of Crystalline Basement Aquifers in Africa Geological Society Special Publication, 66,* 1–27. https://doi.org/10.1144/GSL.SP.1992.066.01.01.